

OUTWARD MIGRATION OF JUPITER AND SATURN IN EVOLVED GASEOUS DISKS

GENNARO D'ANGELO^{1,2,4} AND FRANCESCO MARZARI³

¹ NASA Ames Research Center, MS 245-3, Moffett Field, CA 94035, USA; gennaro.dangelo@nasa.gov

² SETI Institute, 189 Bernardo Avenue, Mountain View, CA 94043, USA; francesco.marzari@pd.infn.it

³ Department of Physics, University of Padova, Via Marzolo 8, Padova I-35131, Italy

Received 2012 May 21; accepted 2012 July 11; published 2012 September 5

ABSTRACT

The outward migration of a pair of resonant-orbit planets, driven by tidal interactions with a gas-dominated disk, is studied in the context of evolved solar nebula models. The planets' masses, M_1 and M_2 , correspond to those of Jupiter and Saturn. Hydrodynamical calculations in two and three dimensions are used to quantify the migration rates and analyze the conditions under which the outward migration mechanism may operate. The planets are taken to be fully formed after 10^6 and before 3×10^6 years. The orbital evolution of the planets in an evolving disk is then calculated until the disk's gas is completely dissipated. Orbital locking in the 3:2 mean motion resonance may lead to outward migration under appropriate conditions of disk viscosity and temperature. However, resonance locking does not necessarily result in outward migration. This is the case, for example, if convergent migration leads to locking in the 2:1 mean motion resonance, as post-formation disk conditions seem to suggest. Accretion of gas on the planets may deactivate the outward migration mechanism by raising the mass ratio M_2/M_1 and/or by reducing the accretion rate toward the star, and hence depleting the inner disk. For migrating planets locked in the 3:2 mean motion resonance, there are stalling radii that depend on disk viscosity and on stellar irradiation, when it determines the disk's thermal balance. Planets locked in the 3:2 orbital resonance that start moving outward from within 1–2 AU may reach beyond ≈ 5 AU only under favorable conditions. However, within the explored space of disk parameters, only a small fraction—less than a few percent—of the models predict that the interior planet reaches beyond ≈ 4 AU.

Key words: accretion, accretion disks – hydrodynamics – methods: numerical – planet–disk interactions – planets and satellites: formation – protoplanetary disks

Online-only material: color figures

1. INTRODUCTION

The architecture of the solar system bears some evidence that Jupiter and Saturn may have been closer to each other in the past (e.g., Malhotra 1993, 1995; Tsiganis et al. 2005; Morbidelli et al. 2005; Gomes et al. 2005). They later moved away from each other because of gravitational interactions with the remnants of the disk of planetesimals from which these planets had formed (e.g., Fernandez & Ip 1984; Hahn & Malhotra 1999). The planetesimal-driven migration of Jupiter and Saturn occurred relatively late, after the gaseous component of the solar nebula had dispersed, and the extent of their radial displacements was probably less than ~ 1 AU (e.g., Franklin et al. 2004; Minton & Malhotra 2009).

Recently, Walsh et al. (2011) proposed a scenario in which orbital migration of Jupiter and Saturn occurred much earlier in the solar system history and was driven by tidal torques in a gas-dominated nebula. The progenitors of Jupiter and Saturn underwent rapid convergent migration toward the Sun, until Saturn became trapped in the 2:3 mean motion resonance with Jupiter. By that time and under the applied conditions, Jupiter had reached ≈ 1.5 AU and Saturn ≈ 2.0 AU. Once the resonant configuration was established, the planets reversed the direction of motion and began migrating outward, preserving the 2:3 commensurability. This scenario may help explain some features of the inner solar system, including the Mars-to-Earth mass ratio and the radial variation of composition in the asteroid belt (see Walsh et al. 2011 for details).

The outward migration is a direct result of the “compact” orbital configuration. Qualitatively, the negative torque balance which would result for a single planet is tipped in favor of the positive torque (from the inner disk) because the negative torque (from the outer disk) is abated by a local reduction of the surface density. This situation requires that the planets be massive enough to significantly perturb, via tidal interaction, the disk's surface density and that their density gaps overlap. These requirements are typically realized if the orbital separation is at most several times the sum of the planets' Hill radii. Therefore, depending on the masses, a (near) 3:2 commensurability is favorable to sustain outward migration of a Jupiter–Saturn pair, whereas for more massive planets, by a factor of about three, a (near) 2:1 commensurability may promote outward migration.

A study by Pierens & Raymond (2011) lends support, under appropriate conditions, to the inward–outward migration scenario of the Jupiter–Saturn system proposed by Walsh et al. (2011). One scope of this paper is to revisit this idea in the context of evolved models of a gas-dominated solar nebula. In particular, we concentrate on the outward migration of a pair of giant planets, whose masses correspond to those of Jupiter and Saturn, after their orbits become locked in the 3:2 mean motion resonance, compatibly with the formation timescales of both Jupiter and Saturn, estimated from core-nucleated accretion models.

We also wish to provide some constraints on the range of radial migration of Jupiter (and Saturn), as a function of the solar nebula properties, under the assumption that the 3:2 orbital resonance is maintained throughout the disk's evolution. Conditions that may break the resonance locking between the two planets or that may inhibit or prevent outward migration are

⁴ Visiting Research Scientist, Los Alamos National Laboratory, Los Alamos, NM 87545, USA.

analyzed as well. In particular, we focus on the process of gas accretion that, on one hand, may alter the planets' mass ratio and, on the other, may reduce the disk density inside the orbit of the interior planet. Both effects act to change the balance of the torques exerted on the planets. In addition, we examine the disk conditions under which convergent migration leads to the capture of the exterior planet in the 1:2 orbital resonance with the interior planet, a configuration that does not promote outward migration of a Jupiter–Saturn pair, and which may leave the planets stranded in the inner disk region. The possibility that Saturn forms within the 1:2 commensurability with Jupiter is also analyzed.

The layout of the paper is as follows. In Section 2, we describe dynamics and thermodynamics of disk models and report on their evolution. In Section 3, the tidal interaction calculations in two and three dimensions are presented, along with the calculations of the migration rates of a 3:2 resonant-orbit pair. Section 4 is dedicated to the long-term orbital evolution of two planets locked in the 3:2 orbital resonance. Two possible effects of gas accretion are analyzed in Sections 5 and 6, while conditions for capture in the 2:1 mean motion resonance and some related issues are examined in Section 7. Section 8 contains the discussion and the summary of the results.

2. LONG-TERM DISK EVOLUTION MODELS

In this section, we describe the dynamics and thermodynamics of solar nebula models. For tested parameters, we report on the disk evolution until the gas is almost entirely dispersed, that is until the disk mass, M_D , is less than 10^{-5} times the mass of the star. By assumption, successful sets of parameters representing a solar nebula model are those that provide a disk lifetime, τ_D , no greater than $\sim 2 \times 10^7$ years. Although the gas mass of disks is notoriously difficult to ascertain, according to observations (see, e.g., reviews by Roberge & Kamp 2010; Williams & Cieza 2011), the presence of gas in the inner regions of protoplanetary disks appears to last $\lesssim 10^7$ years (see also Haisch et al. 2001).

2.1. Disk Dynamics

Consider a gaseous disk orbiting a central star of mass M_s . In the framework of one-dimensional (1D) modeling, we assume azimuthal symmetry around the star and use vertically averaged quantities as a function of the radial distance r . For the current purposes, we assume that the evolution of the disk is driven by viscous torques, \mathcal{T}_v , and wind dispersal, \dot{M}_w at the disk's surface. The torque exerted on a disk ring of radius r , by material orbiting inside the ring, is $\mathcal{T}_v = -2\pi r^3 \nu \Sigma \partial \Omega / \partial r$ (Lynden-Bell & Pringle 1974), where ν is the kinematic viscosity of the gas, Σ the surface density, and Ω the angular velocity. If Ω is identified as the Keplerian velocity (i.e., if effects of gas and magnetic pressure gradients are neglected), then $\mathcal{T}_v = 3\pi \nu \Sigma \mathcal{H}$, where $\mathcal{H} = r^2 \Omega$ is the specific angular momentum of the gas. Along with viscous diffusion, the disk is dispersed by a wind, whose origin is gas photoevaporation from the disk surface produced by photons emitted by the central star. Hence, we write $\dot{M}_w = 2\pi \int \dot{\Sigma}_{pe} r dr$, where $\dot{\Sigma}_{pe}$ is the mass per unit surface area and unit time removed from the disk.

The continuity equation for the disk requires that

$$\frac{\partial}{\partial t} \Sigma + \frac{1}{r} \frac{\partial}{\partial r} (r \Sigma u_r) = -\dot{\Sigma}_{pe}, \quad (1)$$

where u_r is radial velocity of the gas. On the left-hand side, one can recognize the mass per unit time flowing through a

circumference of radius r , $\mathcal{F} = 2\pi r \Sigma u_r$. By using the relation $\mathcal{F} = -\partial \mathcal{T}_v / \partial \mathcal{H}$ (see Lynden-Bell & Pringle 1974) and since we assume Keplerian rotation ($\partial \mathcal{H} / \partial r = r \Omega / 2$), Equation (1) becomes

$$\pi r \frac{\partial}{\partial t} (\Sigma + \Sigma_{pe}) - \frac{\partial}{\partial r} \left(\frac{1}{r \Omega} \frac{\partial \mathcal{T}_v}{\partial r} \right) = 0. \quad (2)$$

To seek for numerical solutions of Equation (2), it is convenient to use \mathcal{H} as an independent variable and $S = \mathcal{H}^3 \Sigma$ as a dependent variable and then solve

$$\frac{\partial}{\partial t} (S + S_{pe}) - \frac{3}{4} (GM_s)^2 \frac{\partial^2}{\partial \mathcal{H}^2} \left(\frac{vS}{\mathcal{H}^2} \right) = 0. \quad (3)$$

In the above equation, G is the gravitational constant and $\dot{S}_{pe} = \mathcal{H}^3 \dot{\Sigma}_{pe}$. Note that the quantity S/\mathcal{H}^2 is the angular momentum per unit surface area. In writing Equation (1), we neglected the effects of the star's growth, which would introduce a term on the right-hand side of the order of $\Sigma \dot{M}_s / M_s$ (see Ruden & Pollack 1991). Given the initial values of \dot{M}_s / M_s considered here (see Section 2.3) and the decline of \dot{M}_s with time, this term would affect Σ only over a timescale of the order of 10^7 years, or longer.

Photoevaporation involves contributions from far-ultraviolet (FUV), extreme-ultraviolet (EUV), and X-ray radiation emitted by the star (see Dullemond et al. 2007; Clarke 2011 and references therein). FUV radiation may be especially important in removing gas at large distances from the star, reducing the gas supply to the inner parts of the disk. However, a self-consistent calculation of FUV photoevaporation rates requires solving for the detailed vertical structure of the disk (e.g., Gorti et al. 2009; Gorti & Hollenbach 2009). Photoevaporation by EUV photons is more tractable since they ionize hydrogen at the very upper layers of the disk. Here we follow a simple approach and adopt the formulation of the EUV photoevaporation rate proposed by Dullemond et al. (2007):

$$\dot{\Sigma}_{pe}^g = \begin{cases} \exp \left[\frac{1}{2} \left(1 - \frac{r_g}{r} \right) \right] \left(\frac{r_g}{r} \right)^2 & \text{for } r \leq r_g, \\ \left(\frac{r_g}{r} \right)^{5/2} & \text{for } r > r_g. \end{cases} \quad (4)$$

The radius $r_g \approx 10 (M_s / M_\odot)$ AU is the gravitational radius, beyond which gas at the disk surface is unbound (see, e.g., Armitage 2011 and references therein). The photoevaporation rate at r_g is

$$\dot{\Sigma}_{pe}^g = 1.16 \times 10^{-11} \sqrt{f_{41}} \left(\frac{1 \text{ AU}}{r_g} \right)^{3/2} \left(\frac{M_\odot}{\text{AU}^2 \text{ yr}} \right), \quad (5)$$

where f_{41} is the rate of EUV ionizing photons emitted by the star in units of 10^{41} s^{-1} . The total mass-loss rate due to photoevaporation is found by integrating Equation (4) over the entire disk according to the definition given above, hence $\dot{M}_w = (0.55977 \sqrt{e} + 4\pi) r_g^2 \dot{\Sigma}_{pe}^g$ or

$$\dot{M}_w = 1.56 \times 10^{-10} \sqrt{f_{41}} \left(\frac{r_g}{1 \text{ AU}} \right) M_\odot \text{ yr}^{-1}. \quad (6)$$

The maximum of $\dot{\Sigma}_{pe}$ occurs at $r = r_g/4$. Locally, gas is removed via photoevaporation and supplied by viscous diffusion, i.e., accretion through the disk, $\dot{M} = -\mathcal{F}$ (note that \mathcal{F}

is positive for an outward transfer of mass). Recalling the relations reported above, we can write $\partial T_v/\partial \mathcal{H} = 3\pi \partial(\nu\Sigma\mathcal{H})/\partial \mathcal{H}$, and thus

$$\dot{M} = 3\pi \left[\nu\Sigma + 2r \frac{\partial}{\partial r}(\nu\Sigma) \right]. \quad (7)$$

For $\nu\Sigma$ nearly independent of r , i.e., in a stationary disk (Pringle 1981; see also Equation (1) with the right-hand side set to zero), $\dot{M} = 3\pi\nu\Sigma$ is nearly constant throughout the disk. Therefore, if $M_s = 1 M_\odot$, we expect gas depletion induced by photoevaporation to occur first around ~ 3 AU.

2.2. Disk Thermodynamics

In order to determine the thermal energy budget of the disk during its evolution, we assume that there is a balance among three terms: viscous heating, irradiation heating by the central star, and radiative cooling from the disk's surface. Viscous dissipation produces an energy flux equal to $Q_v = \nu\Sigma(r\partial\Omega/\partial r)^2$ (see, e.g., Mihalas & Weibel Mihalas 1999), which in the case of Keplerian rotation becomes

$$Q_v = \frac{9}{4} \nu\Sigma\Omega^2. \quad (8)$$

Since $Q_v \propto 1/r^3$, for a disk with $\partial(\nu\Sigma)/\partial r \approx 0$, viscous dissipation becomes an ever less important source of heating as the distance from the star increases.

We follow the formulation of Hubeny (1990) for an irradiated disk and write the energy flux escaping from both sides of the disk surface as

$$Q_{\text{cool}} = 2\sigma_{\text{SB}} T^4 \left(\frac{3}{8}\tau_{\text{R}} + \frac{1}{2} + \frac{1}{4\tau_{\text{P}}} \right)^{-1}, \quad (9)$$

whereas the heating flux arising from stellar irradiation can be written as

$$Q_{\text{irr}} = 2\sigma_{\text{SB}} T_{\text{irr}}^4 \left(\frac{3}{8}\tau_{\text{R}} + \frac{1}{2} + \frac{1}{4\tau_{\text{P}}} \right)^{-1}. \quad (10)$$

In the above equations, σ_{SB} is the Stefan–Boltzmann constant, T the mid-plane temperature, and T_{irr} the irradiation temperature. Note that, for an irradiated disk, the constant in parenthesis on the right-hand side of Equation (9) is generally slightly different from that of a non-irradiated disk (compare with Equation (14) of D'Angelo et al. 2003). As in Menou & Goodman (2004), we set

$$T_{\text{irr}}^4 = (1 - \epsilon) T_s^4 \left(\frac{R_s}{r} \right)^2 W_G, \quad (11)$$

where ϵ is a measure of the disk's albedo, for which we adopt the value 1/2, and T_s and R_s are the effective temperature and radius of the star, respectively. This interpretation of the irradiation temperature, however, neglects the contribution of luminosity released by stellar accretion (e.g., Hartmann et al. 2011). In an actively accreting disk, quantity T_s^4 should be replaced with $T_*^4 = T_s^4 + T_{\text{acc}}^4$, where T_{acc}^4 quantifies the luminosity due to accretion $L_{\text{acc}} = GM_s \dot{M}_s / (2R_s)$ (Pringle 1981) and thus

$$T_{\text{acc}}^4 = \frac{1}{8\pi} \left(\frac{GM_s \dot{M}_s}{\sigma_{\text{SB}} R_s^3} \right), \quad (12)$$

where the accretion rate \dot{M}_s , computed as $-\partial T_v/\partial \mathcal{H}$ (see Section 2.1) at the disk's inner radius, varies with time.

The quantity W_G in Equation (11) is a geometrical factor that accounts for the illumination of disk portions close to (first term) and far from (second term) the star (see Chiang & Goldreich 1997):

$$W_G = 0.4 \left(\frac{R_s}{r} \right) + \frac{H}{r} \left(\frac{d \ln H}{d \ln r} - 1 \right). \quad (13)$$

The adiabatic scale height of the disk, $H = \sqrt{\gamma k_B T / (\mu m_H)} / \Omega$, is derived from the requirement of vertical hydrostatic equilibrium. The adiabatic index, γ , is 1.4, the mean molecular weight, μ , is 2.39, k_B is the Boltzmann constant, and m_H the hydrogen mass.

If the second term on the right-hand side of Equation (13) is negative, the disk is self-shadowed and that term should be dropped. A self-consistent calculation of this term from 1D, vertically averaged models may lead to numerical instabilities (see, e.g., Hueso & Guillot 2005). In fact, meaningful determinations of this term involve solving for the vertical thermal structure of the disk. Therefore, the last term in parenthesis on the right-hand side of Equation (13) is written as η and approximated to 2/7 (see, e.g., D'Alessio et al. 1998; Menou & Goodman 2004; Hueso & Guillot 2005; Rafikov & De Colle 2006).

The optical depths $\tau_{\text{R}} = \kappa_{\text{R}}\Sigma/2$ and $\tau_{\text{P}} = \kappa_{\text{P}}\Sigma/2$ in Equations (9) and (10) are based, respectively, on Rosseland (κ_{R}) and Planck (κ_{P}) mean opacities. Both κ_{R} and κ_{P} depend on T and the mass density $\rho = \Sigma/(2H)$. We adopt grain opacities from Pollack et al. (1994), at temperatures below the vaporization temperatures of silicates, and gas opacities from Ferguson et al. (2005) for solar abundances, when all grain species have evaporated.

The thermal energy budget is given by

$$Q_v + Q_{\text{irr}} - Q_{\text{cool}} = 0. \quad (14)$$

Note that if $Q_v \ll Q_{\text{irr}}$, a situation that may occur in an evolved disk, Equation (14) results in a gas temperature $T = T_{\text{irr}}$, that is,

$$T = T_* \sqrt{\frac{R_s}{r}} [(1 - \epsilon) W_G]^{1/4}. \quad (15)$$

The factor W_G is typically a weakly dependent function of T . If W_G is a constant, then $T \propto r^{-1/2}$. If $W_G \propto R_s/r$ (e.g., at radii $r \sim R_s$), then $T \propto r^{-3/4}$. If $W_G \propto H/r$ (as we assume for $r \gg R_s$), then $W_G^{1/4} \propto T^{1/8}$, the temperature is $T \propto r^{-3/7}$ (see also Chambers 2009), and the disk's aspect ratio is

$$\left(\frac{H}{r} \right)^7 = \eta (1 - \epsilon) \left(\frac{\gamma k_B T_*}{\mu m_H} \right)^4 \left(\frac{R_s}{GM_s} \right)^4 \left(\frac{r}{R_s} \right)^2. \quad (16)$$

The choice of the parameter η may have some impact on the disk's thermal budget, yet Equation (16) suggests that this impact is low.

2.3. Numerical Procedures and Parameters

Equation (3) is evolved in time using an implicit numerical scheme, which avoids the sometimes prohibitively short time steps required by an explicit approach, especially when the inner disk radius extends very close to the star (see Bath & Pringle 1981). We use either a second-order Crank–Nicolson method (e.g., Press et al. 1992) or a fourth/fifth-order Dormand–Prince method with an adaptive step-size control based on the global accuracy of the solution (Hairer et al. 1993). In the latter case,

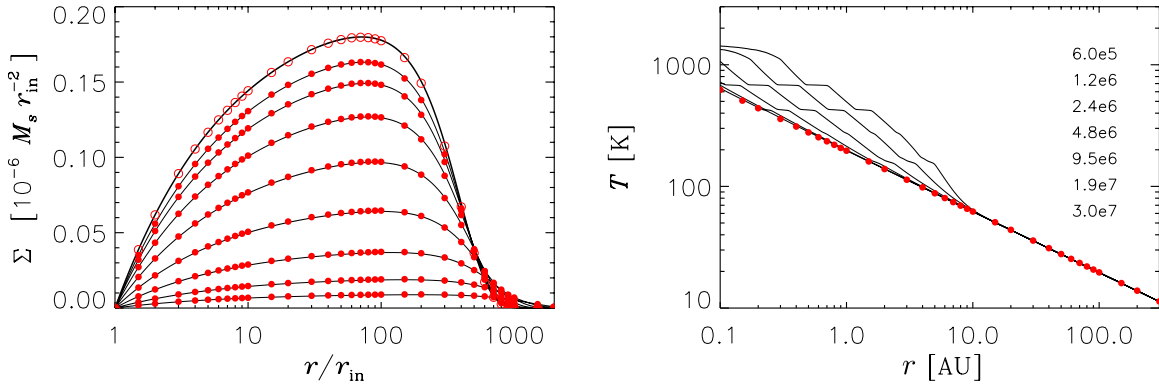


Figure 1. Left: evolution of a viscous disk obtained by solving Equation (3), with $\dot{S}_{pe} = 0$, by means of the Dormand–Prince method. The initial condition (open circles) is the analytic solution of Lynden-Bell & Pringle (1974) for a disk with no central couple, $M_D = 0.1 M_\odot$, $\dot{M}_s = 10^{-7} M_\odot \text{yr}^{-1}$, and $\nu = 8 \times 10^{-6} r_{in}^2 \Omega_{in}$. The solid lines represent the numerical solution at different times and the filled circles are computed using the analytic solution. Right: evolution of temperature obtained by solving Equation (14) for the disk in the left panel. Times in the legend are in years. For testing purposes, W_G is set equal to 0.05. The temperature predicted by Equation (15) is indicated by filled circles.

(A color version of this figure is available in the online journal.)

the evaluation of derivatives (in the Runge–Kutta sequence) is performed by means of a backward Euler (implicit) method. A zero-torque boundary condition, $\mathcal{S} = 0$, is applied at the disk’s inner edge. At the outer edge, the applied boundary condition is such that $\partial \dot{M} / \partial \mathcal{H} = \partial^2 \mathcal{T}_v / \partial \mathcal{H}^2$ is constant. Figure 1 (left) shows a comparison between numerical (lines) and analytic (circles) solutions of Equation (3) (see the figure caption for details).

Equation (14) is solved for the mid-plane temperature, T , at each radius, using a root-finding algorithm based on the Brent’s method (Brent 1973). Convergence of the root-finding process is achieved within a tolerance of 10^{-3} K. An iterative procedure is implemented for each determination of T , so that the applied value of H and that corresponding to the converged temperature do not differ by more than 1%. In Figure 1 (right), the evolution of temperature is shown for the disk considered in the left panel. In this test, we set $W_G = 0.05$, so that the temperature evolves toward that in Equation (15), indicated as filled circles. The temperature profiles show major opacity transitions at $T \approx 160$, 420, 680, and 1400 K, caused by vaporization of, respectively, water ice, refractory organics, troilite, and silicate grains (see Pollack et al. 1994). Note that heating via viscous dissipation is basically confined within ~ 10 AU (see Section 2.2).

The solar nebula extends from $r_{in} = 0.01$ AU to $r_{out} = 1850$ AU and is discretized over 10000 grid points. The large outer radius is chosen to not interfere with viscous spreading of the disk. The numerical resolution is variable and such that $\Delta r / r \simeq 1.2 \times 10^{-3}$. In this study, we assume that $M_s = 1 M_\odot$, $T_s = 4280$ K, and $R_s = 2 R_\odot$ (Siess et al. 2000). The initial surface density distribution of the gas obeys the relation $\Sigma = \Sigma_1^0 (r_1 / r)^\beta$, where $\beta = 1/2$, 1, or $3/2$, within at least ~ 10 AU. Farther away from the star, Σ is exponentially tapered. The extremes of the “slope” β bracket values derived for the solar nebula by Davis (2005) and by Weidenschilling (1977) and Hayashi (1981). The quantity Σ_1^0 , the surface density at $r_1 = 1$ AU, is such that the initial disk mass is $M_D^0 \simeq 0.022$, 0.044, or $0.088 M_s$. (These will be regarded as nominal values. The total initial disk mass differs somewhat for the different values of β because of the tapering procedure.) The photoevaporation rate (Equation (4)) is specified by imposing f_{41} in Equation (5). Here we use $f_{41} = 0.1$, 1, 10, 100, and 1000 (Alexander et al. 2005). The kinematic viscosity is $\nu = \nu_1 (r / r_1)^\beta$ and $\nu_1 = 4 \times 10^{-6}$, 8×10^{-6} , and $1.6 \times 10^{-5} r_1^2 \Omega_1$, where Ω_1 is the rotation rate at $r = r_1$. As a reference, in a disk with constant aspect ratio

$H / r = 0.04$, $\nu_1 = 8 \times 10^{-6} r_1^2 \Omega_1$ corresponds to a turbulence parameter (Shakura & Syunyaev 1973) $\alpha_t = 0.005$. The initial accretion rate onto the star ranges from a few times 10^{-8} to a few times $10^{-7} M_\odot \text{yr}^{-1}$. For comparison, the mass-loss rate in Equation (6) is between $\sim 10^{-10}$ and $\sim 10^{-8} M_\odot \text{yr}^{-1}$.

2.4. Model Results

The majority of disk models have an initial gas inventory of at least $\sim 0.02 M_\odot$ within a distance of 40 AU from the Sun, as required by a canonical minimum mass solar nebula (MMSN; e.g., Weidenschilling 1977; Hayashi 1981). This value is also consistent with the more recent MMSN model adopted by Chiang & Youdin (2010). Due to the steepness of the surface density, disk models with the lowest initial mass and parameter $\beta = 3/2$ have only $0.01 M_\odot$ worth of gas within 40 AU of the Sun.

Gas is removed via the combined action of accretion onto the star, \dot{M} (Equation (7)), and photoevaporation, \dot{M}_w (Equation (6)). In particular, Equation (6) sets an upper limit to dispersal timescale, τ_D , ranging from ~ 1.4 Myr for $M_D^0 \simeq 0.022 M_s$ (when $f_{41} = 1000$) to ~ 560 Myr for $M_D^0 \simeq 0.088 M_s$ (when $f_{41} = 0.1$). For computational purposes, τ_D is defined as the time past which $M_D \lesssim 10^{-5} M_s$.

The evolution of the disk mass for some selected cases is illustrated in Figure 2 for each reference viscosity (see the figure caption for details). A complete list of the disk lifetimes is reported in Table 1. The behavior of the disk mass as a function of time, for the different surface densities, can be qualitatively understood in terms of viscous evolution by means of the analytic solutions of Lynden-Bell & Pringle (1974, their Section 3.3): for equally massive disks, the more compact the disk is (i.e., the larger β), the more rapidly M_D reduces initially. By a somewhat conservative assumption, as discussed above, disks that survive beyond 20 Myr are discarded and will not be given any further consideration. This is the case, for example, for *all* models with a photoionizing rate characterized by $f_{41} \leq 1$ and the flattest initial surface density ($\beta = 1/2$). Models of disks surviving less than 1 Myr will also be discarded based on considerations on planet formation timescales, as explained in Section 4.

A quantity of primary importance for planetary migration is the average surface density around the planet’s orbit. In Figure 3

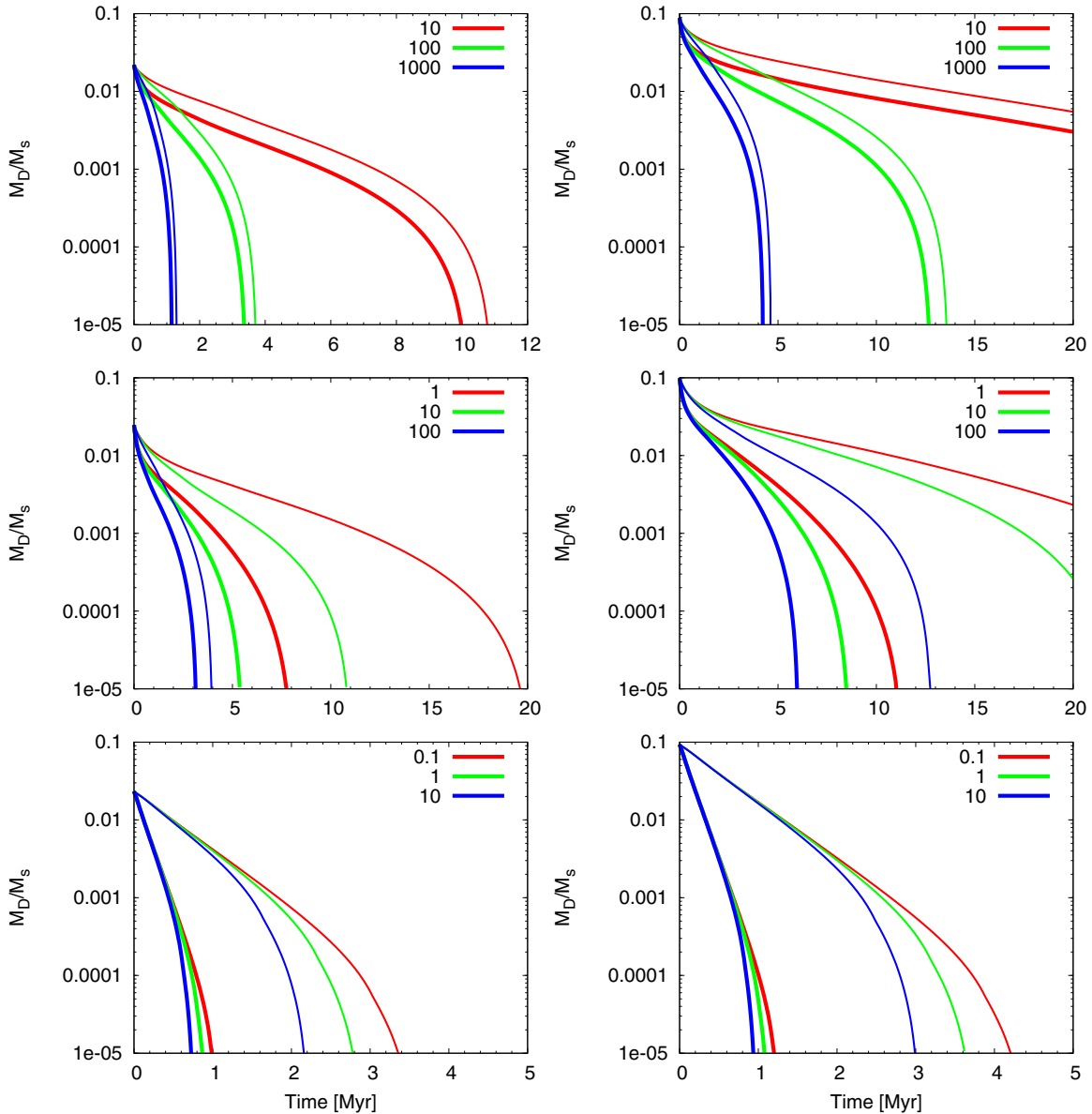


Figure 2. Mass evolution for disks with initial (nominal) masses $M_D^0 \simeq 0.022 M_S$ (left) and $0.088 M_S$ (right). The initial Σ has $\beta = 1/2$ (top), 1 (center), and $3/2$ (bottom). Thin and thick lines represent models with viscosity $\nu_1 = 4 \times 10^{-6}$ and $1.6 \times 10^{-5} r_1^2 \Omega_1$, respectively. Different line styles (line colors) correspond to different rates of EUV ionizing photons emitted by the star in units of 10^{41} s^{-1} , as reported in the legends.

(A color version of this figure is available in the online journal.)

(left panels), the evolution of Σ is shown for cases with different values of parameters β and f_{41} . As anticipated at the end of Section 2.1, once the accretion rate drops below some threshold, photoevaporation produces a gap in the surface density at a radial distance of a few AU. Then the disk inside the gap is removed by viscous diffusion on a timescale of the order of $r^2/(2\pi\nu)$ orbital periods. We shall see in the Sections 3.2 and 3.3 that the disk's aspect ratio has also a large impact on the rates and direction of migration. In the right panels of Figure 3, H/r is plotted at reference times for the same models as in the left panels. Once Σ becomes small enough and the viscous heating term Q_v in Equation (14) becomes unimportant, the disk temperature, and hence H/r (see Section 2.2), is dictated only by the stellar irradiation temperature (Equation (11)).

The surface density at 1 AU, Σ_1 , versus time is illustrated in Figure 4 for selected models from Table 1. Thin and thick lines refer to smallest and largest values of ν_1 , respectively. To

obtain a better statistical characterization of the disk density and temperature, for each pair of parameters (M_D^0 , β) listed in Table 1, ν_1 and f_{41} are varied randomly in the corresponding ranges indicated in the table, for a total of more than 2000 realizations. The histogram in Figure 5 (left) shows that after ~ 1 Myr the value of Σ_1 is 150 g cm^{-2} , or less, in $\sim 80\%$ of the models that may represent the solar nebula. The right panel of Figure 5 illustrates the occurrence frequency of the mid-plane temperature at 1 AU. As a reference, the equilibrium temperature established by stellar irradiation alone, i.e., Equation (15), is $T_1 \approx 100 \text{ K}$.

3. TIDAL INTERACTIONS OF JUPITER AND SATURN WITH THE DISK

The evolution of the thermodynamical quantities (principally Σ , T , and H/r) of solar nebula models, obtained in the previous

Table 1
Lifetimes from Disk Models

M_D^0/M_s	ν_1^c	τ_D^a								
		$\beta^b = 1/2$			$\beta = 1$			$\beta = 3/2$		
		$f_{41}^d = 10$	100	1000	1	10	100	0.1	1	10
0.022	4×10^{-6}	10.8	3.70	1.31	19.6	10.8	3.92	3.35	2.78	2.21
0.022	8×10^{-6}	10.3	3.50	1.24	12.6	8.01	3.75	1.84	1.57	1.25
0.022	1.6×10^{-5}	9.95	3.35	1.16	7.75	5.38	3.12	0.98	0.87	0.74
0.044	4×10^{-6}	20.8	7.05	2.46	25.6	16.2	7.55	3.78	3.20	2.57
0.044	8×10^{-6}	20.1	6.72	2.32	15.7	10.9	6.31	2.05	1.78	1.48
0.044	1.6×10^{-5}	19.5	6.47	2.22	9.36	6.90	4.50	1.09	0.98	0.83
0.088	4×10^{-6}	40.5	13.5	4.66	31.8	21.9	12.7	4.21	3.63	3.00
0.088	8×10^{-6}	39.3	13.1	4.43	19.0	13.9	9.07	2.26	1.99	1.69
0.088	1.6×10^{-5}	38.5	12.6	4.25	11.0	8.47	5.97	1.20	1.08	0.93

Notes.

^a Time past which $M_D \lesssim 10^{-5} M_s$, in units of Myr.

^b Initial “slope” of the disk’s surface density.

^c Kinematic viscosity at $r_1 = 1$ AU in units of $r_1^2 \Omega_1 = (GM_s r_1)^{1/2}$.

^d Rate of EUV ionizing photons emitted by the star in units of 10^{41} s^{-1} (see Equation (5)).

section, can be used to evaluate the range of orbital migration of a pair of planets, over the disk lifetime, once appropriate migration rates are supplied. In this section we derive such rates.

3.1. 2D and 3D Hydrodynamical Calculations

The migration of a Jupiter–Saturn pair in a gaseous disk is evaluated by using a combination of two-dimensional (2D) and three-dimensional (3D) hydrodynamical calculations of tidal interactions between the planets and the disk. We adopt a reference frame $\{O; r, \theta, \phi\}$ with origin, O , fixed on the star, radius ranging from 0.25 to 7 AU, and azimuth varying between 0 and 2π . In the 2D disk approximation, the co-latitude angle θ is equal to $\pi/2$, whereas it varies from θ_{\min} to $\pi/2$ in a 3D disk. In the latter case, the disk opening angle, θ_{\min} , is such that the disk’s vertical extent locally comprises at least three pressure scale heights, H . Mirror symmetry with respect to the $\theta = \pi/2$ plane is imposed on account of the planets orbiting in this plane of symmetry. The surface density Σ initially has a dimensionless gradient $d \ln \Sigma / d \ln r = -1/2$. We work in the assumption that the disk is locally isothermal, i.e., the temperature depends only on r , and that H/r is a constant. The gas pressure is therefore proportional either to Σ/r (2D) or to ρ/r (3D), where ρ is the mass density. It is further assumed that the kinematic viscosity of the disk, ν , is constant throughout the disk.

The coordinate system rotates about the axis perpendicular to the planets’ orbital plane ($\theta = 0$ axis) at a variable rotation speed, $\Omega_f = \Omega_f(t)$. Both Ω_f and $\dot{\Omega}_f$ are imposed by the requirement that the (relative) azimuthal position of the interior planet, ϕ_1 , remains constant in time and the (relative) angular velocity, $\dot{\phi}_1$, is zero (for details about the procedure, see D’Angelo et al. 2005).

Naming \mathbf{r}_1 and \mathbf{r}_2 the vector positions of the interior (Jupiter) and exterior planet (Saturn), respectively, the gravitational potential in the disk is

$$\Phi = -\frac{GM_s}{r} - \frac{GM_1}{\sqrt{|\mathbf{r} - \mathbf{r}_1|^2 + \varepsilon_1^2}} - \frac{GM_2}{\sqrt{|\mathbf{r} - \mathbf{r}_2|^2 + \varepsilon_2^2}} + \frac{GM_1}{r_1^3} \mathbf{r} \cdot \mathbf{r}_1 + \frac{GM_2}{r_2^3} \mathbf{r} \cdot \mathbf{r}_2, \quad (17)$$

which accounts for the contributions of non-inertial terms due to the reference frame being centered on the star (see Nelson et al. 2000). The potential softening lengths ε_1 and ε_2 are set equal to 1/4 (or 1/7 in some calculations) times the Hill radius, R_H , of the corresponding planet. It is worth stressing that the argument according to which ε should be a fraction of the disk’s scale height, H , in the 2D geometry (e.g., Masset 2002; Müller et al. 2012) applies to fully embedded planets, when $R_H < H$. If $R_H \gtrsim H$, as in all our 2D calculations, the local disk scale height depends also on the gravity of the planet itself (e.g., D’Angelo et al. 2003). In such cases, one physical constrain on ε is that it should be smaller than the radius over which gas is effectively bound to (i.e., it rotates about) the planet ($\sim R_H/3$; see, e.g., D’Angelo et al. 2003).

The Navier–Stokes equations that characterize the disk evolution are solved by means of the finite-difference code described in D’Angelo et al. (2005 and references therein) with modifications detailed below. The disk is discretized in $678 \times 16 \times 700$ grid zones, in r , θ , and ϕ , respectively (and 678×700 in 2D). Calculations were also performed at a higher resolution of $1353 \times 28 \times 2096$. Comparisons of the evolution of the planets’ orbital elements at these two resolutions yield good agreement. We apply the wave-damping boundary conditions of de Val-Borro et al. (2006) within $r = 0.3$ and beyond $r = 6.65$ AU, which are appropriate for planets far enough from the boundaries.

We implemented an orbital advection algorithm along the lines of the FARGO algorithm of Masset (2000; see also Kley et al. 2009). These types of algorithms exploit periodicity properties of the flow, as those naturally occurring in the azimuthal direction of a disk. (Note that these algorithms can also be applied to local disk simulations, if periodicity is imposed at the patch boundaries; see Gammie 2001.) As demonstrated by Masset (2000), when the highest velocity component is along the periodic direction, in a 2D disk such techniques can increase the time step limit required by the Courant–Friedrichs–Lewy condition (see, e.g., Stone & Norman 1992), relative to a standard advection scheme, by factors ~ 10 or larger. In a 3D disk, the gain may critically depend on

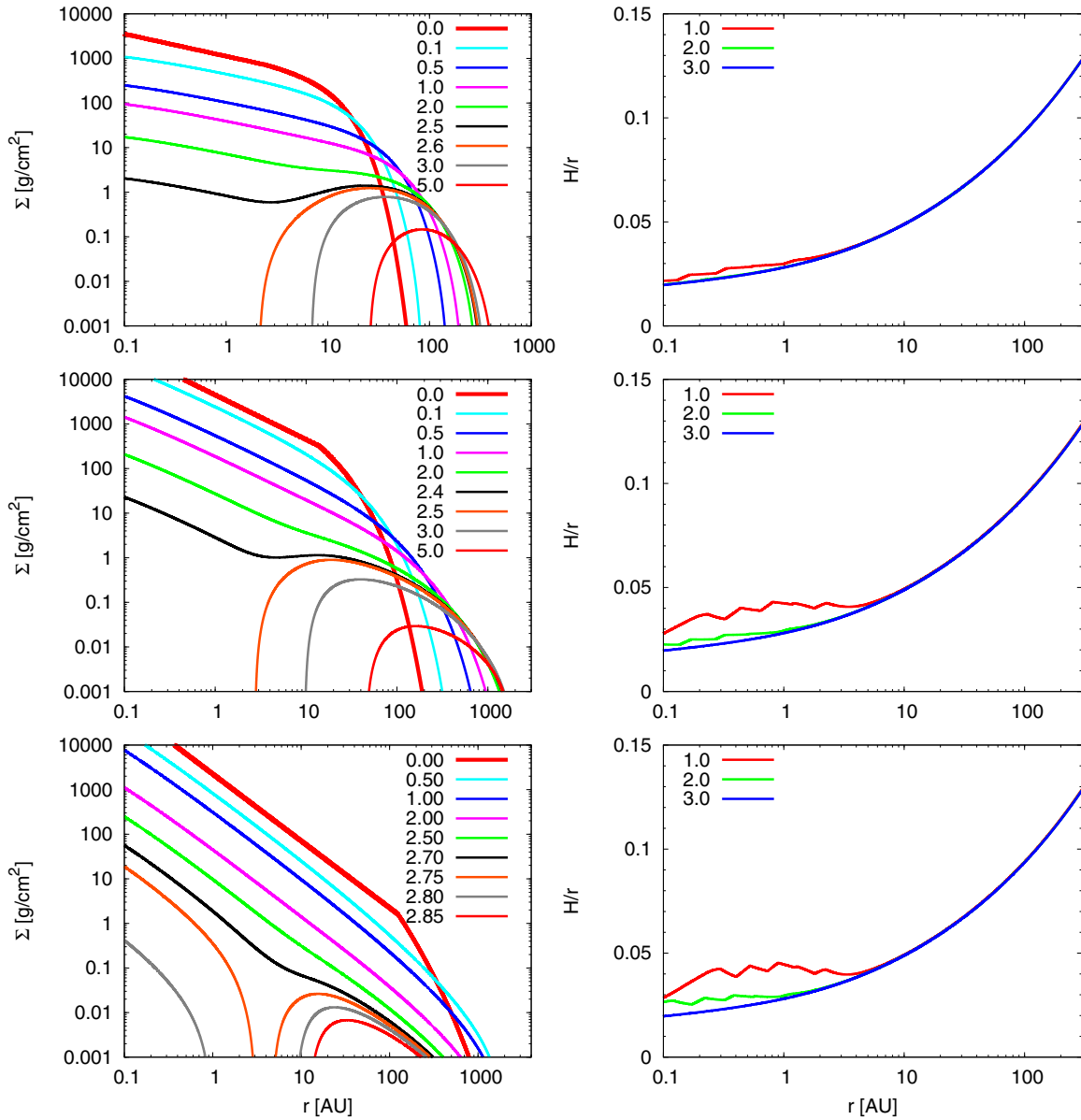


Figure 3. Evolution of the disk's surface density (left) and disk's relative thickness (right) of disk models with $v_1 = 8 \times 10^{-6} r_1^2 \Omega_1$, $M_D^0 \simeq 0.022 M_s$, $f_{41} = 10$, and $\beta = 1/2$, (top), $v_1 = 8 \times 10^{-6} r_1^2 \Omega_1$, $M_D^0 \simeq 0.088 M_s$, $f_{41} = 100$, and $\beta = 1$ (center), and $v_1 = 4 \times 10^{-6} r_1^2 \Omega_1$, $M_D^0 \simeq 0.044 M_s$, $f_{41} = 1$, and $\beta = 3/2$ (bottom). Times indicated in the legend are in Myr.

(A color version of this figure is available in the online journal.)

the numerical resolution in the vertical (θ) direction.⁵ The implementation requires care when handling the transport of quantities defined on staggered meshes. Kley et al. (2009) use split cells, apply the transport algorithm to each part, and then recombine the partial information to reconstruct the full transport. Unlike them, we define the auxiliary variables required in the procedure (see Masset 2000 for details) on the same staggered meshes as the transport quantities are defined, wherever they are necessary. This approach requires more copies of the standard auxiliary variables to be defined, and hence more memory storage, but offers the advantage that the advection of all hydrodynamical quantities can be performed in a single step.

⁵ Since a disk is typically thin, very high resolutions can be more easily achieved in the vertical direction. In a viscous disk, the time step constraint required by the diffusion part of Navier–Stokes equations scales as the square of the grid spacing. This requirement, at high resolution and high viscosity, can severely reduce (or even nullify) the benefits of orbital advection.

Contrary to the implementations of both Masset (2000) and Kley et al. (2009), the algorithm used here avoids any directional bias, maintaining the full symmetry of the advection scheme, by using a sequence that alternates the transport among directions (see Stone & Norman 1992).

The equations of motion of two planets orbiting in a disk around a star, written in a reference frame rotating at variable angular speed, are

$$\ddot{\mathbf{r}}_1 = -\frac{G(M_s + M_1)}{r_1^3} \mathbf{r}_1 - \frac{GM_2}{r_2^3} \mathbf{r}_2 - \frac{GM_2}{r_{12}^3} \mathbf{r}_{12} + \mathcal{A}_1 - \mathcal{A}_s - \boldsymbol{\Omega}_f \times (\boldsymbol{\Omega}_f \times \mathbf{r}_1) - 2 \boldsymbol{\Omega}_f \times \dot{\mathbf{r}}_1 - \dot{\boldsymbol{\Omega}}_f \times \mathbf{r}_1 \quad (18)$$

$$\ddot{\mathbf{r}}_2 = -\frac{G(M_s + M_2)}{r_2^3} \mathbf{r}_2 - \frac{GM_1}{r_1^3} \mathbf{r}_1 + \frac{GM_1}{r_{12}^3} \mathbf{r}_{12} + \mathcal{A}_2 - \mathcal{A}_s - \boldsymbol{\Omega}_f \times (\boldsymbol{\Omega}_f \times \mathbf{r}_2) - 2 \boldsymbol{\Omega}_f \times \dot{\mathbf{r}}_2 - \dot{\boldsymbol{\Omega}}_f \times \mathbf{r}_2, \quad (19)$$

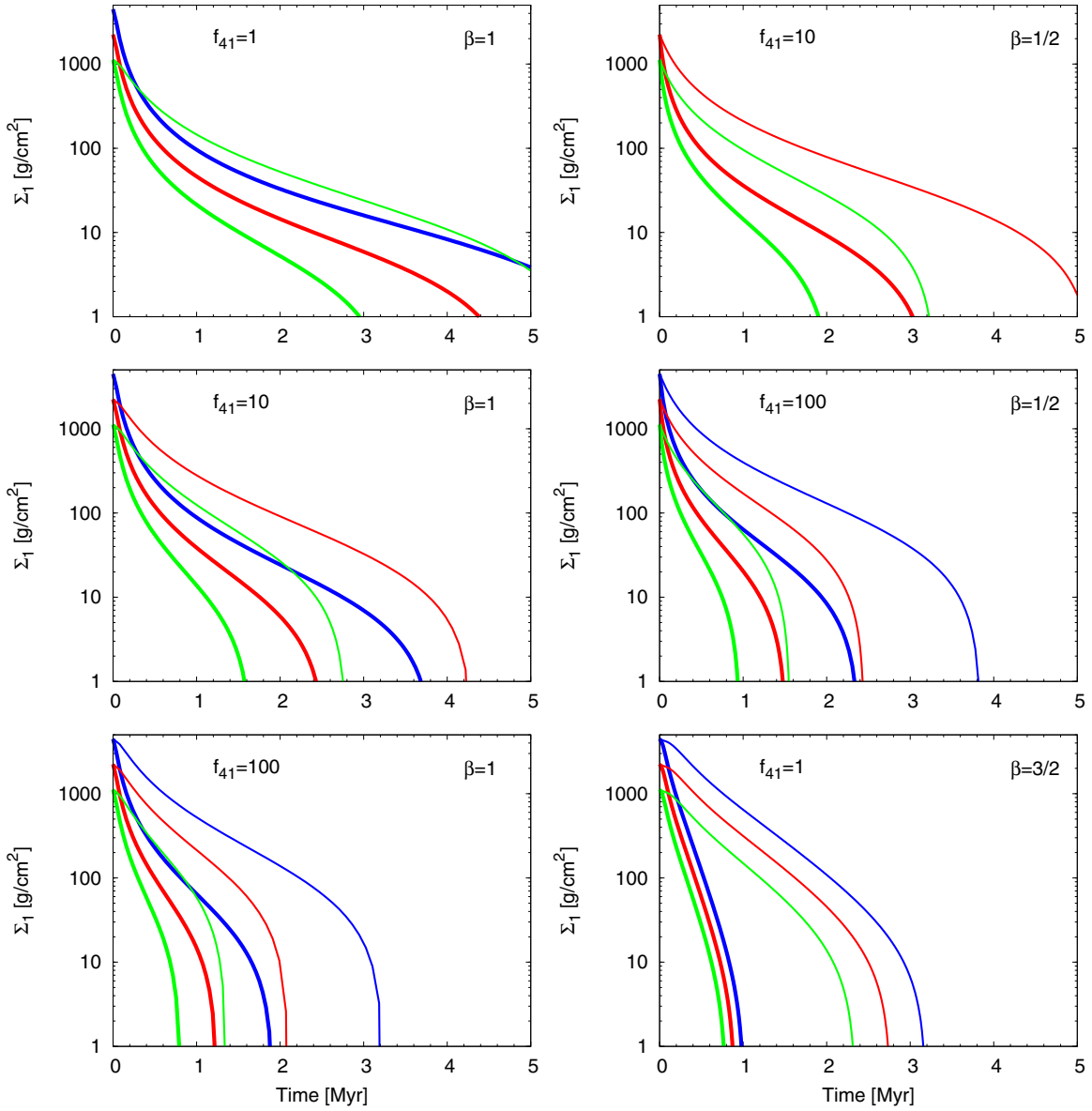


Figure 4. Evolution of the disk's surface density at 1 AU. Thin and thick lines represent models with viscosity $\nu_1 = 4 \times 10^{-6}$ and $1.6 \times 10^{-5} r_1^2 \Omega_1$, respectively. Different line styles (line colors) correspond to different disk's initial masses. The value of the EUV ionizing photon rate, f_{41} , and of the initial surface density gradient, β , are given in each panel.

(A color version of this figure is available in the online journal.)

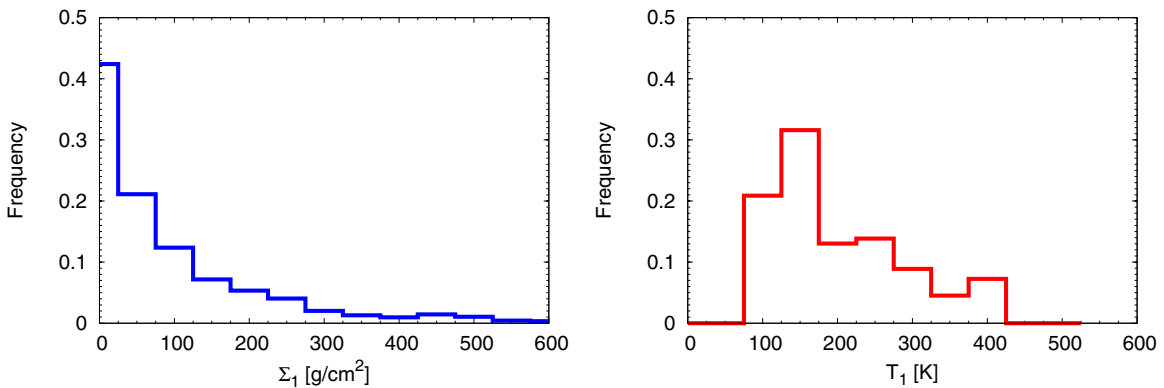


Figure 5. Histograms of the surface density (left) and mid-plane temperature (right) at 1 AU, at time $t \approx 1$ Myr for disk models whose lifetime τ_D is longer than 1 Myr and shorter than about 20 Myr. The histograms are based on over 2000 models using a random selection of ν_1 and f_{41} , for each pair (M_D^0, β) listed in Table 1, in the respective ranges indicated in the table.

(A color version of this figure is available in the online journal.)

where $\mathbf{r}_{12} = \mathbf{r}_1 - \mathbf{r}_2$. Note that since the origin of the coordinate system is on the star, Equations (18) and (19) include the forces per unit mass exerted on the star by the planets. The gravitational acceleration terms imposed by the disk, \mathcal{A}_1 , \mathcal{A}_2 , and \mathcal{A}_s , are defined by Equations (8) and (9) of D'Angelo et al. (2005) and updated every hydrodynamical time step, Δt . Equations (18) and (19) are integrated numerically over Δt by means of a high-order Gragg–Bulirsch–Stoer extrapolation algorithm with order and step-size control (Hairer et al. 1993). The algorithm chooses automatically a suitable order at each (internal) step, which basically depends on the required tolerance of the solution error. We set a relative tolerance of 10^{-9} and an absolute tolerance of 10^{-14} .

3.2. Torque Calculations and Outward Migration

The basic mechanism that may allow a pair of resonant-orbit planets to experience a positive torque exerted by a gaseous disk and migrate outward was first described by Masset & Snellgrove (2001). Labeling with subscripts 1 and 2 the inner and outer planet, respectively, in order for this mechanism to be active, the following conditions must be fulfilled.

1. The planet-to-star mass ratios ($q_i = M_i/M_s$) must be such that $q_1 > q_2$.
2. The separation of the semimajor axes $\Delta a = a_2 - a_1$ must be such that $\Delta a = b(R_{H,1} + R_{H,2})$, where $b \lesssim 4.5$ (as we shall discuss below).
3. q_2 must be large enough to open a gap, or partial gap, in the density distribution by tidal torques.

Condition (2) above implies that $\Delta a/a_1 = (\sqrt[3]{q_1} + \sqrt[3]{q_2})/(\sqrt[3]{3/b} - \sqrt[3]{q_2})$. However, Hill stability for close planets on circular orbits also imposes that $\Delta a/a_1 \gtrsim 2.40 \sqrt[3]{q_1 + q_2}$ (this inequality strictly applies in the limit of vanishing masses and absence of gas; see Gladman 1993), whose right-hand side is about equal to 0.26 for $q_1 = M_1/M_s = 9.8 \times 10^{-4}$ and $q_2 = M_2/M_s = 2.9 \times 10^{-4}$, hence $b \gtrsim 2$ (or 2.2, adopting a more precise determination of the Hill stability criterion; see Gladman 1993, for details; see also Figure 6). Conditions (1) and (2) suggest that, for a Jupiter–Saturn pair, the first encountered first-order mean motion resonance in which the mechanism may be activated is the 3:2 (the second-order 5:3 commensurability being another possibility), as indicated in Figure 6. In principle, configurations external, but sufficiently near, to resonances may also promote outward migration, as we shall see in Section 3.3. It is worth stressing here that simple capture in a mean motion resonance does not imply outward migration (see, e.g., Zhang & Zhou 2010), as we shall see in Section 7.

Figure 7 (top and middle) illustrates the surface density perturbed by resonant-orbit planets, derived from 3D calculations for disks of different thicknesses (see the figure caption). The bottom panels of the figure show the mass density in a vertical slice of the disk, while the planets are aligned with the star. The exterior planet opens a partial gap in the case of a thinner disk, but it does so to a lesser extent in the other case (see bottom panels).

The occurrence of outward migration of resonant-orbit planets can be intuitively understood from Figure 8, which reports on the results obtained from the same calculations as in Figure 7, where Saturn is caught in a 2:3 mean motion resonance with Jupiter. The azimuthally averaged surface density in normalized units (long-dashed lines) indicates that Saturn has cleared a partial gap, whose inner part overlaps with the outer part of the gap opened by Jupiter. The short-dashed lines in the

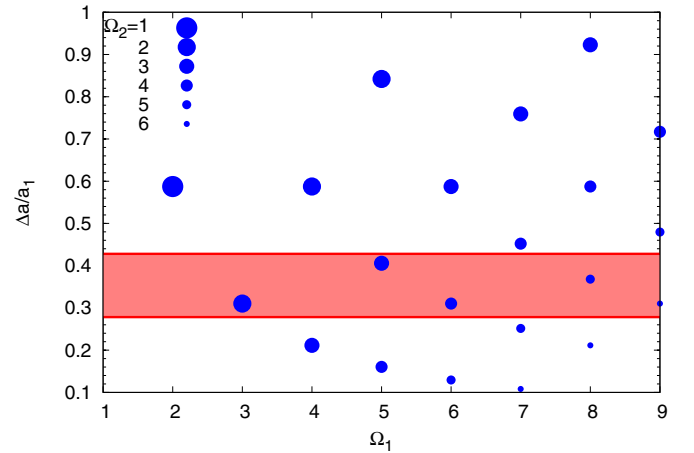


Figure 6. Fractional difference, $\Delta a/a_1 = a_2/a_1 - 1$, between the semimajor axes of the interior (a_1) and exterior (a_2) planets, as a function of the mean motion of the interior planet Ω_1 (in scaled units). Different symbol sizes refer to different mean motions of the exterior planet, Ω_2 (see the legend). The region of the graph below the shaded area is unstable due to planet–planet interaction. The Hill stability criterion adopted in this figure is given by Equation (23) of Gladman (1993). The region above the shaded area does not fulfill condition (2) for gap overlap (see also Figures 7 and 8). Resonant orbits falling in the shaded area may activate outward migration.

(A color version of this figure is available in the online journal.)

figure represent torque density distributions (D'Angelo & Lubow 2008, hereafter DL08) due to Jupiter, dT/dM . These functions yield the total torque when integrated over the disk mass. The torque exerted on the interior planet peaks at $a_1 \pm R_{H,1}$ and is mostly comprised in a radial region of average width $\sim 3.5 R_{H,1}$ on either side of the orbit (note that $R_{H,1} > H$ in the case displayed in the left panel and $R_{H,1} \approx H$ in the other case). But since gas depletion due to gap formation may extend somewhat beyond this distance (see long-dashed lines in Figure 8), one may allow for a maximum value of the factor b in condition (2) above between 4 and 5. It is also important to notice that the orbital eccentricity of a planet acts to widen and smooth out gap edges (see, e.g., Figure 2 of D'Angelo et al. 2006), which may also affect somewhat the factor b .

The solid lines in Figure 8 represent the cumulative torque, which is defined as

$$\mathcal{T}_{\text{CM}}(r) = 2\pi \int_0^r \frac{dT}{dM}(\Sigma)r'dr'. \quad (20)$$

Looking at \mathcal{T}_{CM} in the left panel of Figure 8, it appears to be clear that the positive torque exerted by the disk interior of Jupiter's orbit is larger than that exerted by the disk exterior of the orbit, principally because Saturn has lowered the density there. The right panel illustrates the situation for a thicker disk, in which gas depletion operated by the exterior planet is not sufficient to reverse the sign of the torque. Figure 9 allows for a comparison of the cumulative torque for three different values of the disk thickness: $H/r = 0.04$ (top), 0.05 (center), and 0.07 (bottom) (see the figure caption for further details). A closer inspection of dT/dM and \mathcal{T}_{CM} in Figure 8 (left) and of the cumulative torque in Figure 9 (top) indicates that the total (positive) torque is basically driven by Lindblad resonances and that corotation torques are unimportant (\mathcal{T}_{CM} does not vary significantly over the radial width of the corotation region), as also argued by Morbidelli & Crida (2007).

It thus appears from Figures 8 and 9 that the discriminant factor for outward, stalled, or inward migration is the depth

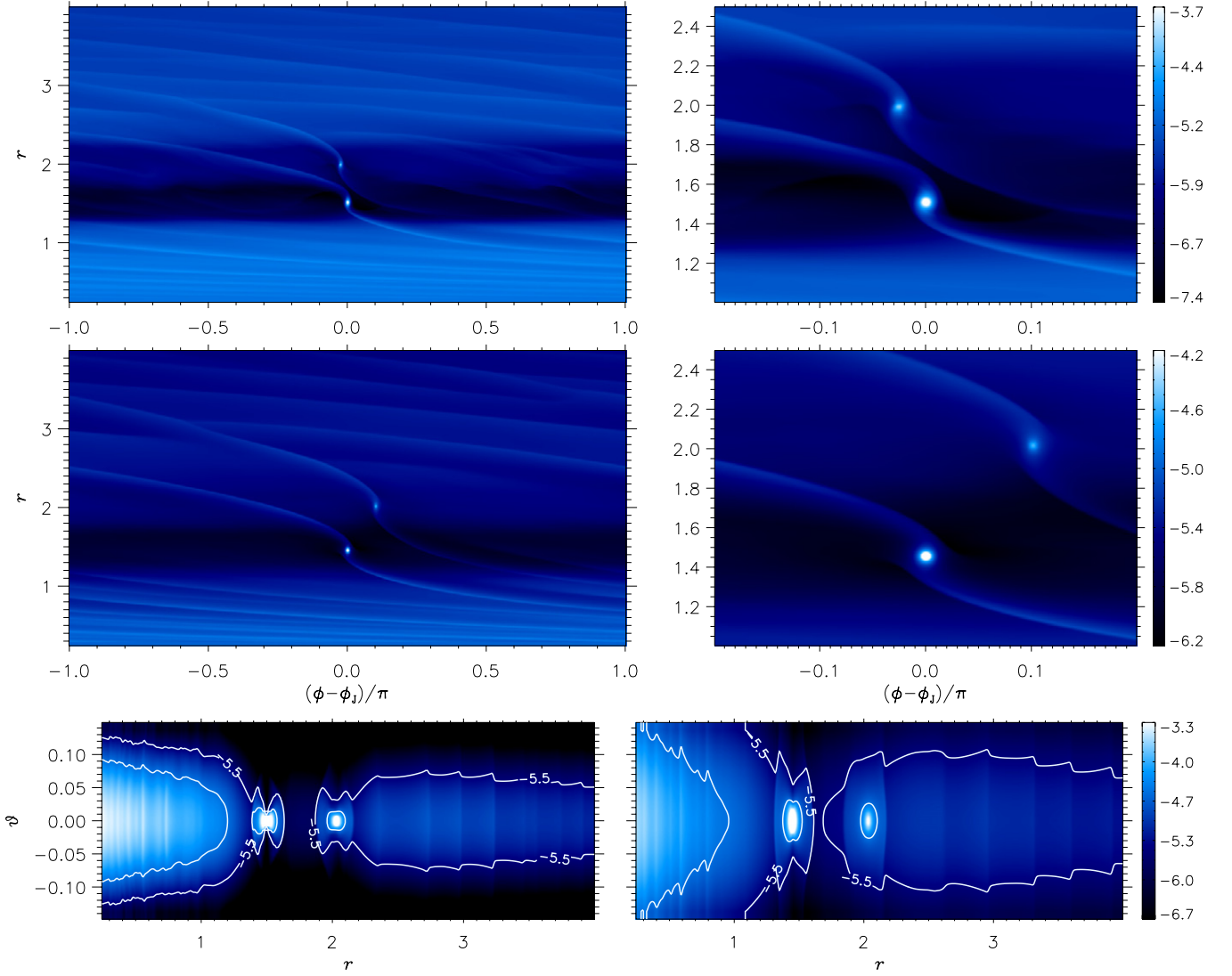


Figure 7. Surface density distribution obtained from 3D calculations of a disk with $H/r = 0.04$ (top) and 0.07 (middle). The angle ϕ_j is the azimuth of the interior planet, Jupiter. The turbulence parameter α_1 is 0.005 in both cases. A zoom of the region around the planets is shown in the right panels. The gray scale (color scale) is logarithmic and given in units of $M_s r_1^{-2}$, where r_1 indicates the radius $r = 1$ (i.e., the unit of length). The bottom panels show the vertical stratification of the mass density, ρ , at the disk azimuth $\phi_j = \phi_s$ for $H/r = 0.04$ (left) and 0.07 (right). The angle $\vartheta = \pi/2 - \theta$ is the disk's latitude and the gray scale (color scale) is in units of $M_s r_1^{-3}$.

(A color version of this figure is available in the online journal.)

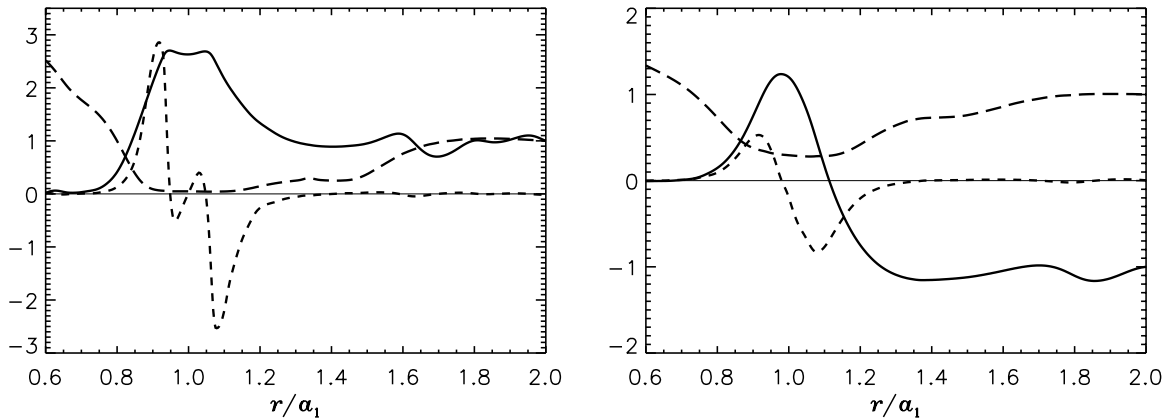


Figure 8. Azimuthally averaged surface density (long-dashed line), torque per unit disk mass (short-dashed line) exerted on the inner planet, and cumulative torque (Equation (20)) acting on the inner planet (solid line) for the same models as in Figure 7 (cases with $H/r = 0.04$ and 0.07 on the left and right, respectively). Quantity dT/dM is normalized to $10^3 GM_s (M_1/M_s)^2/a_1$ (a_1 is the semimajor axis of the interior planet). The surface density and cumulative torque are normalized by their absolute values at $r/a_1 = 2$. The peaks occurring at the planets' orbital radii (due to mass accumulation within the Roche lobe) have been removed from the surface density profile. Results displayed here were obtained from 3D calculations and averaged over a few orbital periods of the outer planet.

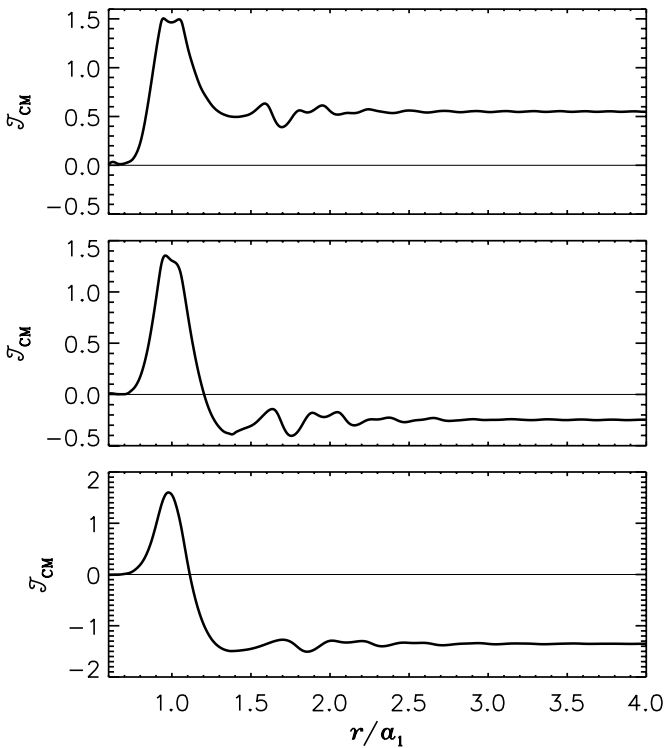


Figure 9. Cumulative torque, Equation (20), exerted on the interior planet by a 3D disk for which the turbulence parameter is $\alpha_t = 0.005$ and the thickness is $H/r = 0.04$ (top), 0.05 (center), and 0.07 (bottom). Quantity \mathcal{T}_{CM} is normalized to $10^{-3} G M_s^2 (M_p/M_s)^2 / a_1$, where a_1 is the semimajor axis of the interior planet.

(and width) of the outer planet’s gap. If the outer planet opened a very deep and sufficiently wide gap, the inner planet would be subjected only to a one-sided Lindblad (positive) torque exerted by the interior disk that, to within a factor of order unity, can be written as (see Lubow & Ida 2010 and references therein)

$$\mathcal{T}_{\text{OS}} \sim a^4 \Omega^2 \Sigma \left(\frac{M_p}{M_s} \right)^2 \left(\frac{a}{\tilde{\Delta}} \right)^3, \quad (21)$$

where $\tilde{\Delta} = \max(H, R_H)$. The concept of one-sided torque is very useful to evaluate the presence of a tidally induced gap, i.e., condition (3) above. To first-order approximation, a density depletion begins to form when the one-sided torque exceeds the viscous torque (see Section 2.1), $\mathcal{T}_{\text{OS}} \gtrsim \mathcal{T}_v$, which yields a simple order-of-magnitude condition $q^2 \gtrsim 3\pi\alpha_t (H/a)^2 (\tilde{\Delta}/a)^3$ (see also Papaloizou & Lin 1984; Ward & Hahn 2000), or

$$g = \frac{q}{\sqrt{3\pi\alpha_t}} \left(\frac{a}{H} \right) \left(\frac{a}{\tilde{\Delta}} \right)^{3/2} \gtrsim 1. \quad (22)$$

This conditions should be regarded as a measure of how much the density along the planet’s orbit is depleted, hence it can be considered a condition for gas depletion. A condition for tidal truncation (gap formation) is then $g \gg 1$ (see also Lin & Papaloizou 1986b). If predictions from the inequality (22) are compared with results from direct 3D calculations (DL08, Figures 6 and 8), one finds that $g \approx 1$ corresponds to a $\sim 20\%$ density depletion (relative to the unperturbed state, i.e., with no planet), and $g \approx 2.7$ to $\sim 60\%$ depletion. If applied to Saturn in the disks of Figure 8, $g \approx 3.4$ for a density depletion of roughly 75% (left panels) and again $g \approx 1$ for a density drop of $\sim 20\%$ (right panels).

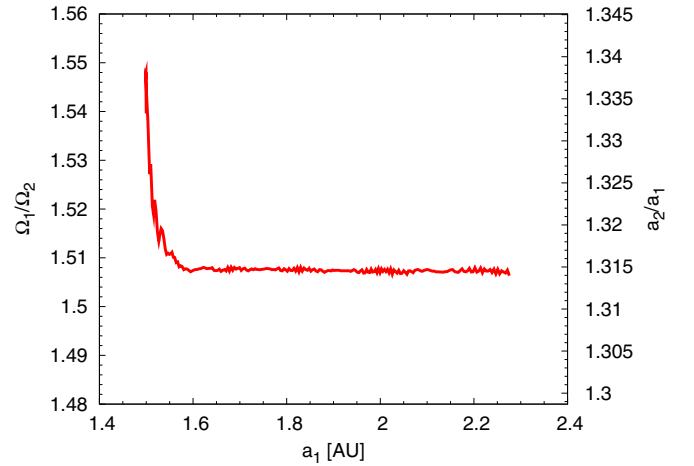


Figure 10. Ratio of orbital frequencies of the inner to the outer planet showing convergence toward the 3:2 commensurability and subsequent resonant-orbit migration. The direction of migration of both planets is outward. The labels on the right vertical axis are an approximation of the semimajor axis ratio, a_2/a_1 . (A color version of this figure is available in the online journal.)

3.3. Orbital Migration Rates

In order to derive migration rates, we shall assume that the orbits of the interior and exterior planets, Jupiter and Saturn, respectively, are in the 3:2 mean motion resonance and that this resonance is maintained during migration. Results from a calculation that support this assumption are plotted in Figure 10. All calculations resulting in outward migration behave similarly, but there are also instances in which the resonance is broken (see below). Since the ratio a_2/a_1 is supposed to be a constant, we concentrate on the migration rate of the interior planet, Jupiter. We seek an expression for \dot{a} of the form

$$\frac{da}{dt} = \dot{a}_{\text{ref}} k_1(\Sigma) k_2(a) k_3(g), \quad (23)$$

where \dot{a}_{ref} is a reference migration speed, and k_1 , k_2 , and k_3 are dimensionless functions. To derive such expression, we employ results from both 2D and 3D calculations. In this section, the planets are fully formed since the beginning of the calculations and non-accreting.

In Figure 11 (top-left panel), the semimajor axis evolution of the reference model is shown for both planets (see the figure caption for details). The disk has an aspect ratio $H/r = 0.04$ and turbulence parameter $\alpha_t = 0.005$. At $r = 1$ AU, the surface density is $\Sigma_1 = 50 \text{ g cm}^{-2}$ at time $t = 0$. This value is chosen from the disk evolution calculations discussed in Section 2.4, which show that $\gtrsim 50\%$ of disks have $\Sigma_1 \lesssim 50 \text{ g cm}^{-2}$ after ~ 1 Myr. Following Pierens & Raymond (2011), we set $a_1 = 1.5$ AU and $a_2 = 2$ AU at $t = 0$ (see the caption of Figure 11 for further details), slightly outside the 3:2 mean motion resonance (see Figure 10). In the top-right panel of the figure, a comparison between 2D and 3D calculation results is presented. The 3D migration rate is about 25% smaller than the 2D one, which correction we apply to all 2D results. Note that this comparison is carried out at the same numerical resolution in the $r-\phi$ plane (see Section 3.1). The parameter that may produce the largest differences between 2D and 3D outcomes is the disk thickness. In this case, however, we rely only on 3D calculations to approximate Equation (23). Similar plots are shown in the bottom panels of Figure 11, but for the orbital eccentricity. For the duration of the evolution we consider, the eccentricity of

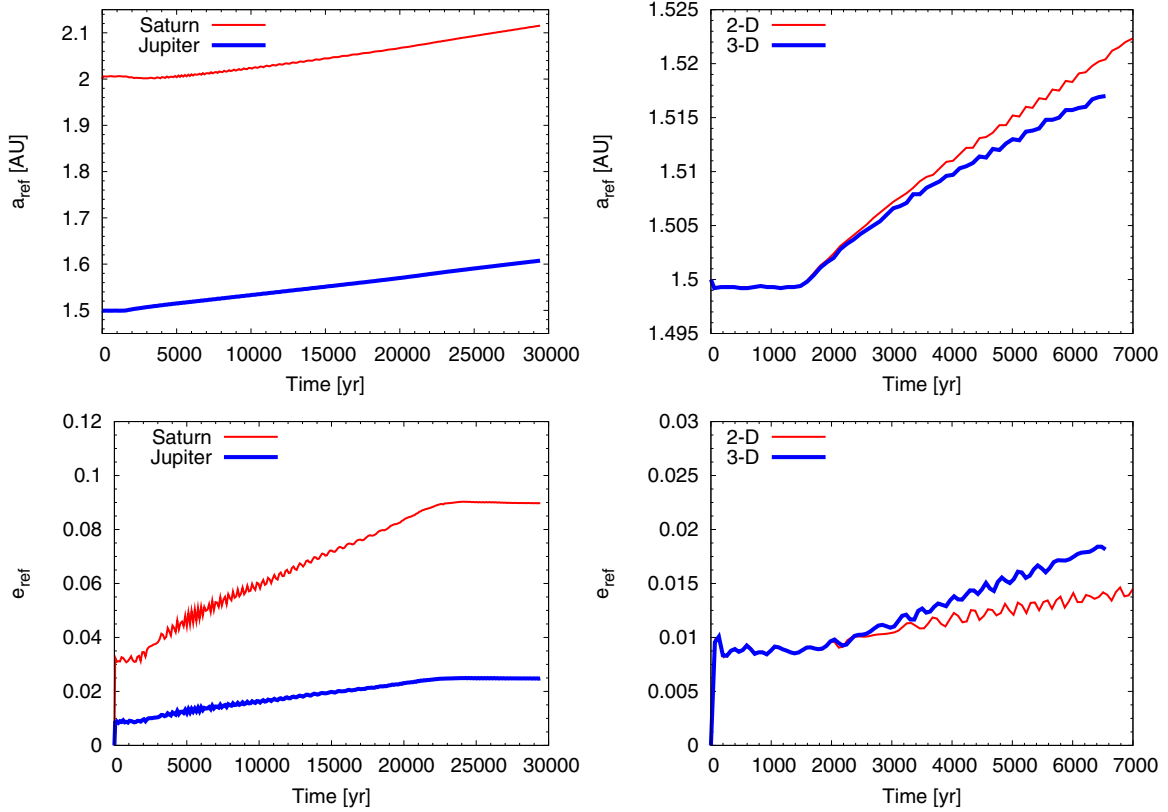


Figure 11. Left: semimajor axis (top) and eccentricity (bottom) evolution of a Jupiter–Saturn system locked in the 3:2 mean motion resonance, for the reference model. The planets evolve in a disk with $H/r = 0.04$, $\alpha_t = 0.005$, and an initial Σ at 1 AU of 50 g cm^{-2} . During the first 1500 years, the planets interact with each other and with the star, but do not “feel” the disk. Elliptical (osculating) orbital elements are obtained applying Gauss perturbation equations (e.g., Beutler 2005) in a non-rotating frame (including perturbations from the other planet) and then averaging over 60 and 40 orbital periods of the inner and outer planet, respectively. Right: comparison between evolutions of the semimajor axis (top) and eccentricity (bottom) of Jupiter, obtained for the reference model, in a 2D and 3D disk. (A color version of this figure is available in the online journal.)

Jupiter does not exceed ~ 0.03 in any of the models discussed in this section. The orbital eccentricity of the exterior planet grows larger, to values $e_2 \sim 0.1$ (see also Pierens & Raymond 2011).

As mentioned above, Figures 10 and 11 indicate that outward migration can be activated also if orbital configurations are external, but somewhat near, the 3:2 commensurability. This effect is related to the gap widths and the extent to which density perturbations compound. In this context, orbital eccentricity may play some important role, since it affects the shape of a gap (D’Angelo et al. 2006).

In Section 3.2, we argued that the torque exerted on Jupiter would tend to the one-sided Lindblad torque \mathcal{T}_{OS} (Equation (21)), if Saturn (i.e., the exterior planet) carved a very deep and wide gap in the disk. In the opposite limit of very large disk thickness, H , and/or viscosity parameter, α_t , neither Jupiter nor Saturn would be capable of depleting the disk significantly and therefore it is expected that the torque exercised upon the interior planet will be of *type I* (Ward 1986; Lin & Papaloizou 1986a)

$$\mathcal{T}_I \sim -a^4 \Omega^2 \Sigma \left(\frac{a}{H} \right)^2 \left(\frac{M_p}{M_s} \right)^2, \quad (24)$$

where, again, we neglect a factor (typically) of the order of unity in front of the right-hand side. Since both \mathcal{T}_{OS} and \mathcal{T}_I are linear in Σ , and since in the limit of zero orbital eccentricity

$$\frac{da}{dt} = \frac{2\mathcal{T}}{a\Omega M_p}, \quad (25)$$

one obvious guess is to approximate k_1 as a linear function. In the left panel of Figure 12, the migration velocity \dot{a} of the inner planet from calculations (symbols), normalized to the velocity from the reference model (Figure 11), is plotted against the value of the normalized Σ . Here the value of the surface density is that at a distance of $5.5 R_{H,1}$ from the (inner) planet’s orbit and interior to it. A function proportional to Σ (solid line) appears a reasonable approximation of k_1 over the range of densities shown in the figure. Hence, we will assume that $k_1(\Sigma) = \Sigma/\Sigma_{\text{ref}}$, where the density is sampled as stated above.

We note in passing that if the interior, and hence the exterior, planet is subjected to a torque of the type given in Equation (24), the resonance may be broken since the inner, more massive planet may drift inward at larger speed than the outer, less massive planet. This is indeed observed in some calculations of relatively thick disks, as illustrated in Figure 13 (see the figure caption for further details).

The form of function k_2 can be guessed following a similar line of argument. In their natural units of $a^2 \Omega^2$ (times a mass), both torques \mathcal{T}_{OS} (Equation (21)) and \mathcal{T}_I (Equation (24)) scale as $a^2 \Sigma$ (the dependence on H/a is considered later), which can be seen as a measure of the local disk mass. Therefore, if Σ was constant, $\dot{a} \propto a^2$ in units of $a\Omega$ (see Equation (25)) and thus \dot{a} would scale as $a^{3/2}$. In the right panel of Figure 12, the migration speed of the inner planet from calculations (symbols), normalized to the reference migration speed, is plotted as a function of a , normalized to the semimajor axis in the reference model, a_{ref} . Also in this case, the approximation

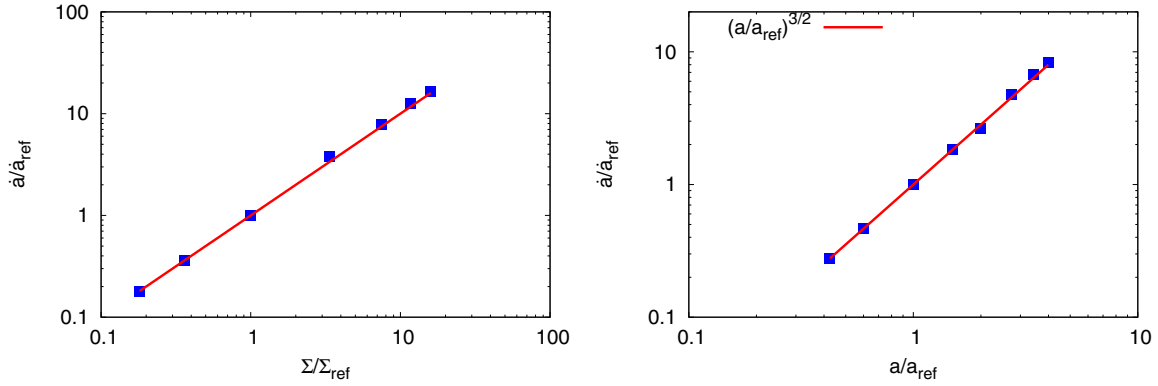


Figure 12. Normalized migration speed $\dot{a}/\dot{a}_{\text{ref}}$ vs. the normalized (azimuthally averaged) surface density $\Sigma/\Sigma_{\text{ref}}$ (left) and vs. a/a_{ref} (right). The surface density is sampled at $a_1 = 5.5 R_{\text{H},1}$. All of the calculations are run for an evolution time between 10^4 and $\gtrsim 2 \times 10^4$ years. To determine \dot{a} , first $a(t)$ is averaged in time over several tens of years and then a linear fit to the data is performed using a base time span of one to several thousand years. (A color version of this figure is available in the online journal.)

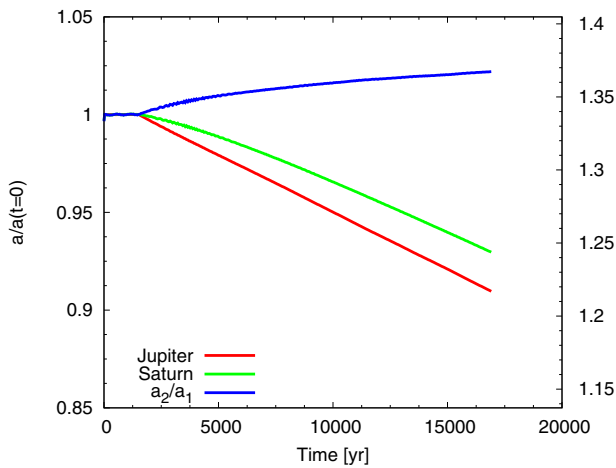


Figure 13. Semimajor axes vs. time of a Jupiter–Saturn type system evolving in a 3D disk with $H/r = 0.07$, $\alpha_t = 0.005$, and an initial Σ at 1 AU of 50 g cm^{-2} . Each semimajor axis is normalized to its initial value. The planets are subjected to disk torques after the first 1500 years. The planets undergo divergent inward migration.

(A color version of this figure is available in the online journal.)

seems satisfactory (solid line) and so we shall assume that $k_2(a) = (a/a_{\text{ref}})^{3/2}$.

In Section 3.2, it was anticipated that the depth and width of the density depletion produced by the exterior planet play a fundamental role in determining magnitude and direction of the interior planet’s migration, and hence of the pair as a whole. Quantity g (Equation (22)) can be used as a proxy to discriminate among the various situations, i.e., different combinations of H/r and α_t (and q) that may affect Σ . On account of the compact orbital configuration, since $q_1 > q_2$ we have that $g_1 > g_2$ (unless H/r and/or α_t are rapidly varying with disk radius). If $g_2 \gg 1$, then $g_1 \gg 1$, and the interior planet is likely subjected to a torque whose limit is the one-sided Lindblad torque in Equation (21) and the two planets migrate outward. Otherwise, if $g_1 \ll 1$, then $g_2 \ll 1$, and migration will be dictated by a type I torque (Equation (24)) and be directed inward.

The migration velocity of the inner planet should depend on both g_1 and g_2 . However, in the present context g_2 should have the larger impact of the two and therefore, for the sake of simplicity, we assume that function k_3 depends only on g_2 . In particular, referring to the value of g_2 in the reference model (Figure 11) as g_{ref} and indicating g_2 simply as g , k_3 will be approximated as a function of g/g_{ref} . Since it is unclear how the

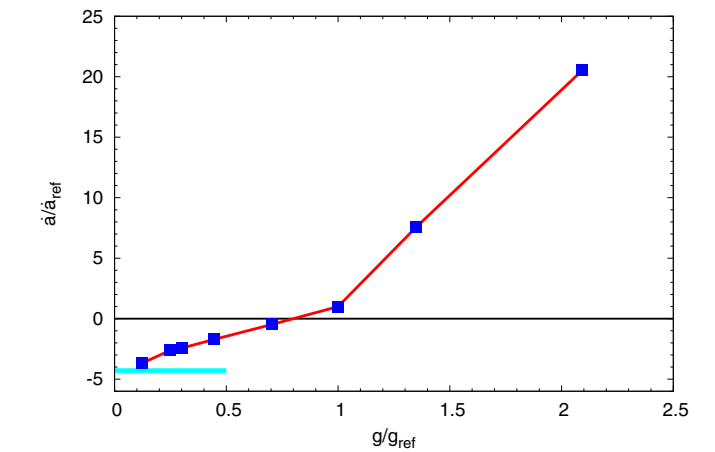


Figure 14. Normalized migration speed $\dot{a}/\dot{a}_{\text{ref}}$ for various values of the ratio g/g_{ref} , calculated for the exterior planet, according to Equation (27). All of the models are run for an evolution time of between 6×10^3 and 1.2×10^4 years. The thick horizontal line segment represents the type I migration speed that would apply to the inner planet if $H/r = 0.1$, corresponding to the value used for leftmost data point on the graph. For reference, the normalized migration speed corresponding to the one-sided torque in Equation (21) would be ~ 90 . The broken line is a linear interpolation of the data, which will be used as a representation of k_3 .

(A color version of this figure is available in the online journal.)

agreement between 2D and 3D calculations varies as a function of the disk thickness (it should likely worsen as H increases), we only use 3D calculations to find an approximation to function k_3 . Figure 14 shows the ratio $\dot{a}/\dot{a}_{\text{ref}}$ obtained from calculations for various values of the ratio g/g_{ref} . The thick horizontal line in the plot indicates the type I migration speed that would apply to the inner planet if $H/r = 0.1$, corresponding to the value used for leftmost data point on the graph. For reference, the normalized migration speed corresponding to the one-sided torque in Equation (21) would be ~ 90 . The broken line is a linear interpolation of the data, which will be used as a representation of k_3 .

3.4. Approximation of the 3:2 Resonant-orbit Migration Velocity

Summarizing the results of Section 3.3, we write the migration speed of the interior planet as

$$\frac{da}{dt} = \dot{a}_{\text{ref}} \left(\frac{\Sigma}{\Sigma_{\text{ref}}} \right) \left(\frac{a}{a_{\text{ref}}} \right)^{3/2} k_3(g/g_{\text{ref}}), \quad (26)$$

where the dimensionless function k_3 is obtained via linear interpolation of the numerical data in Figure 14, i.e., the thick

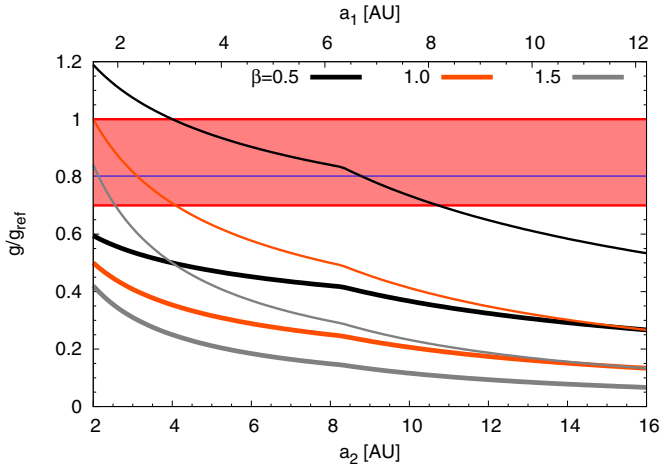


Figure 15. Ratio g/g_{ref} (Equation (27)) as a function of the exterior (bottom axis) and interior (top axis) planet's orbital radius. Here, H/r is approximated by Equation (16). The shaded area indicates the region where \dot{a}_1 changes sign: $\dot{a}_1 > 0$ ($\dot{a}_1 < 0$) above (below) the shaded area. The horizontal line within the boundaries of the shaded area is the nominal value for stalling migration (see the text). The various curves represent g/g_{ref} for different “slope” parameters, β (see the legend). Thin and thick curves correspond to $\nu_1 = 4 \times 10^{-6}$ and $1.6 \times 10^{-5} r_1^2 \Omega_1$, respectively.

(A color version of this figure is available in the online journal.)

solid line in the figure. The reference values in Equation (26) are taken from the reference model, corrected for 3D effects, as discussed in Section 3.3: $\dot{a}_{\text{ref}} = 2.7 \times 10^{-6} \text{ AU yr}^{-1}$ for $\Sigma_{\text{ref}} = 42 \text{ g cm}^{-2}$ and $a_{\text{ref}} = 1.57 \text{ AU}$. Recall that both Σ and Σ_{ref} are evaluated at a distance of $5.5 R_{\text{H},1}$ interior of the inner planet's orbit. The argument of function k_3 is given by

$$\frac{g}{g_{\text{ref}}} = \sqrt{\frac{\alpha_{1,\text{ref}}}{\alpha_1}} \left(\frac{H_{\text{ref}}}{H} \right) \left(\frac{R_{\text{H}}}{\tilde{\Delta}} \right)^{3/2}, \quad (27)$$

where $\alpha_{1,\text{ref}} = 0.005 \sqrt{1 \text{ AU}/a_{\text{ref}}}$, $(H/a)_{\text{ref}} = 0.04$, and $\tilde{\Delta} = \max(H, R_{\text{H}})$. Recall that here parameters g and g_{ref} are computed from Equation (22) are applied to the exterior planet. For a mass ratio q different from that of the reference model, the right-hand side of Equation (27) should be multiplied by q/q_{ref} . Equation (26), without the correction due to 3D effects, is also in reasonable agreement with the results presented by Pierens & Raymond (2011) in their Figure 21, for a disk of $0.4 M_{\text{J}}$ within 1.5 AU ($\Sigma \sim 500 \text{ g cm}^{-2}$ at 1 AU). As explained above, the exterior planet's orbit may not always be resonant with that of the interior planet, when migration is inward (see Figure 13). Nonetheless, for the outer planet's orbit we set $a_2 = (3/2)^{2/3} a_1$.

Equation (26) predicts stalling points (where k_3 , and hence \dot{a} , is ≈ 0) at $g_0 \approx 0.8 g_{\text{ref}}$, which will be regarded as a nominal value. But, notice that since the approximation to k_3 is sampled at a limited number of points, its zero could be located at a somewhat different abscissa, yet it is located between $0.7 g_{\text{ref}}$ and g_{ref} . In principle, there could be multiple stalling points in a disk (if disk properties are not monotonic), which would represent locations of stable equilibrium since they are convergent radii for the planets' semimajor axes. The argument, however, is based on the assumption that the 3:2 commensurability is preserved even for inward migration. This is not true in general (as illustrated, for example, in Figure 13), but it further requires that the inward migration of the exterior planet be faster than that of the interior planet and that the condition for gap overlap (see condition (2) in Section 3.2) be satisfied. When these conditions are not met, the pair of planets

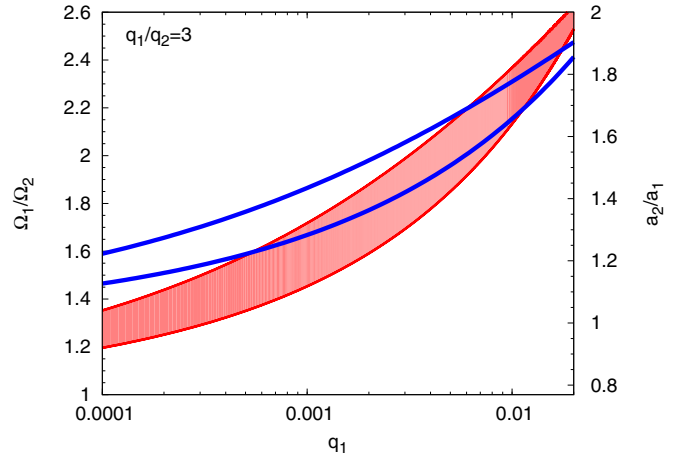


Figure 16. Shaded area represents orbital frequency ratios, as a function of the interior planet mass, which may possibly activate outward migration of a pair of planets whose mass ratio is such that $q_1/q_2 = M_1/M_2 = 3$. The upper boundary of the shaded area is given by condition (2) of Section 3.2. The lower boundary is given by a Hill stability criterion for circular orbit planets (Equation (23) of Gladman 1993), in absence of gas. It is assumed that parameter g , defined in Equation (22) and applied to the exterior planet, is large enough to allow for sufficient gas depletion. The area bounded by the thicker lines represents this condition in terms of the ratio a_2/a_1 (labeled on the right vertical axis).

(A color version of this figure is available in the online journal.)

can migrate past a stalling point, toward the star. This may happen, for example, if disk temperature and viscosity are low enough so that both planets open up a gap and drift according to *type II* migration before capture into resonance occurs.

Some constraints on the range of outward migration predicted by Equation (26) can be derived for the disk models discussed in Section 2.4. The disk thickness, H , is affected by internal (viscous) heating typically over the first few million years of evolution (see Figure 3, left). If we neglect that source of heating, H can be approximated by using Equation (16) and then Equation (27) can provide a rough measure of a disk's radial range over which the planets can drift away from the star, as shown in Figure 15. The addition of internal heating would raise the value of H , hence reducing the ratio g/g_{ref} , which suggests that outward migration may not be activated in the warm interiors of a young disk. The radial region over which a curve extends above or, to some degree, inside the shaded area is favorable to outward migration. The intersection of a curve with the horizontal line in the shaded area gives the nominal radius of the stalling point of each planet (see above). According to the plot, outward migration of a Jupiter-mass planet locked in the 3:2 mean motion resonance with a Saturn-mass planet cannot proceed beyond $\sim 7 \text{ AU}$ (*top x-axis*). The numerical experiments discussed in Section 4 are broadly consistent with this prediction.

The validity of Equation (26) for planet-to-star mass ratios different from those adopted here ($q_1 = M_1/M_s = 9.8 \times 10^{-4}$ and $q_2 = M_2/M_s = 2.9 \times 10^{-4}$) was not investigated. Parameter g (Equation (22)) is $\propto q_2$ if $R_{\text{H}} < H$ and $\propto \sqrt{q_2}$ otherwise. Therefore, a faster outward migration might be expected as q_2 increases, provided that the ratio q_1/q_2 stays roughly constant. Condition (2) of Section 3.2, along with the requirement of Hill stability, suggests that, as q_2 increases beyond ~ 0.001 , the 2:1, rather than the 3:2, commensurability may be available to activate outward migration for a ratio $q_1/q_2 \approx 3$, in accord with the findings of Crida et al. (2009). This is schematically illustrated in Figure 16 (see the figure caption for further details).

As the ratio q_1/q_2 approaches 1, the shaded area in the graph shifts upward.

4. LONG-TERM 3:2 RESONANT-ORBIT MIGRATION OF JUPITER AND SATURN

The results from the disk models of Section 2.4 can be combined with the results of Section 3.4 to study the migration of a resonant-orbit pair of planets with masses corresponding to those of Jupiter and Saturn. Here we shall assume that, by a time τ_p , both planets have fully formed, i.e., they have reached their final masses, and their orbits have become locked in the 3:2 mean motion resonance. Planet formation calculations of a giant planet via core nucleated accretion (e.g., Hubickyj et al. 2005; Alibert et al. 2005; Lissauer et al. 2009; Movshovitz et al. 2010; Mordasini et al. 2011) indicate that the formation time of Jupiter is greater than ~ 1 Myr, although this timescale is affected by the formation of the solid core and thus by the distance where the core forms. The formation of Saturn, the exterior planet, seemingly takes somewhat longer (see, e.g., Pollack et al. 1996; Dodson-Robinson et al. 2008; Benvenuto et al. 2009). In addition to the formation time, there is the time required by convergent orbital migration to bring the planets into mean motion resonance (which is also included in τ_p). Assuming that τ_p is determined mainly by the formation time and for lack of better constraints, we choose three reference times τ_p of 1, 2, and 3 Myr (e.g., Kenyon & Bromley 2009; Bromley & Kenyon 2011).

It is important to bear in mind that longer timescales are possible, whereas it is unclear if shorter timescales are feasible. In fact, there are also observational constraints suggesting that Jupiter formed after several million years (see Scott 2006 and references therein).

The disk evolution models presented in Section 2.4 are recalculated, starting from time τ_p and using Equations (26) and (27), to integrate the orbital radius of the interior planet. The orbit of the exterior planet is constrained by the 2:3 resonant-orbit requirement with the interior planet (see Section 3.4). In particular, the disk models provide the quantities Σ , α_t , and H , used in Equations (26) and (27), as they evolve over time. The effects of the torques exerted by the planets on the disk are not taken into account in the 1D models because, for current purposes, the feedback of the tidal field on the disk and its effects on the migration rates are included in the 2D and 3D calculations discussed above. The mass of both planets is constant, but we will contemplate the impact of gas accretion in Section 5. Since $\tau_p \geq 1$ Myr, useful disk models are those for which $\tau_D > 1$ Myr (and $\lesssim 20$ Myr).

The evolution of a_1 , the interior planet's orbital radius, is illustrated in Figure 17 for selected cases (see the figure caption for details). The complete list of the asymptotic values of a_1 , a_∞ , is reported in Table 2 for $\tau_p = 1$ Myr. In some cases, the orbital radius remains nearly unchanged. This happens as a result of Σ (around $r \sim a_1$) being too low, at time $t = 1$ Myr, for any significant amount of angular momentum to be transferred to/from the disk. Obviously, this result holds for $\tau_p > 1$ Myr.

The outcomes of Figure 17 and Table 2 can be interpreted with the aid of Figure 15. For the highest viscosity regime, outward migration is not activated, and both planets migrate inward regardless of other disk parameters. At the intermediate viscosity, \dot{a}_1 may be positive, but the nominal stalling radius is within 2 AU, hence the interior planets may not proceed beyond this distance. The lowest viscosity regime offers the widest range of outward migration, resulting in nominal stalling

radii of ≈ 6.5 AU ($\beta = 1/2$), ≈ 2.4 AU ($\beta = 1$), and ≈ 1.6 AU ($\beta = 3/2$). Because of the variation of ν with radius, as the density steepens, the nominal stalling radius moves inward. At even smaller viscosity, migration of the resonant pair may proceed to larger distances, but in this case there are at least two possible issues that may arise. One is related to the disk lifetime, which increases as ν decreases (see Table 1). The other is related to the mode of migration of the exterior planet prior to resonance capture, which may transition to type II at low enough viscosity, hence convergent migration toward the interior planet may be compromised (see Section 7).

Figure 15 can also assist in extending the results illustrated in Figure 17, and reported Table 2, to different initial orbital radii. Assuming that viscous heating does not represent a major source term in the energy budget, Equation (14), a pair of planets that become locked in the 3:2 mean motion resonance inside the stalling radii (of each planet) will migrate toward those locations. Whether or not the planets may reach those radii depends on the gas density level in the disk. At $\nu_1 = 4 \times 10^{-6} r_1^2 \Omega_1$, models for which $a_\infty \approx 6.5$ AU for $\beta = 1/2$, or ≈ 2.4 AU for $\beta = 1$, or ≈ 1.6 AU for $\beta = 3/2$, have reached their stalling radii. If the pair becomes locked into resonance outside the stalling radii, the planets will converge toward, or transit across, them depending on the disk conditions (see discussion in Section 3.4).

Among the sets of parameters listed in Table 2, only five are compatible with the outward migration of the interior planet beyond ~ 5 AU (when resonance locking occurs at ~ 1 AU). Only two sets of parameters remain compatible with this requirement if the formation timescale is $\tau_p = 2$ Myr, and only one if $\tau_p = 3$ Myr, as illustrated in the left panel of Figure 18 (see the figure caption for further details).

In order to derive a distribution of the asymptotic orbital radii of the interior planet, a_∞ , for each pair of values (M_D^0 , β) listed in Table 2, ν_1 and f_{41} are varied randomly between the corresponding minimum and maximum values reported in the table, and τ_p is varied randomly between 1 and 3 Myr. A total of over 1200 models were computed and the histogram of the results is shown in the right panel of Figure 18. Overall, there is a 97% probability that the interior planet will achieve an asymptotic radius $a_\infty \lesssim 3$ AU and a 98% probability that $a_\infty \lesssim 4$ AU.

5. GAS ACCRETION AND PLANET GROWTH

As mentioned in Section 3.2, the first condition necessary to activate the outward migration mechanism of resonant-orbit planets is that the interior planet's mass must exceed that of the exterior planet. In the limit of equal mass planets, one expects the outer Lindblad torque exerted on the exterior planet to overcome the inner Lindblad torque exerted on the interior planet (see, e.g., Morbidelli & Crida 2007). Several outcomes are then possible, including breaking of the resonance, scattering, and inward type II migration of both planets.

The neglect of gas accretion, especially on the exterior planet, represents possibly the most serious limitation of this mechanism. Hydrodynamical calculations can provide maximum, or disk-limited, gas accretion rates for such planets. Although they do not necessarily represent the actual accretion rates, formation models of Jupiter (Lissauer et al. 2009) indicate that once runaway accretion begins, a giant planet does grow at a disk-limited accretion rate. In a disk with $H/r \lesssim 0.05$ and $\alpha_t \lesssim 0.005$, an *isolated* Saturn-mass planet may accrete gas at a rate a few times as large as that of a Jupiter-mass planet at the same location in

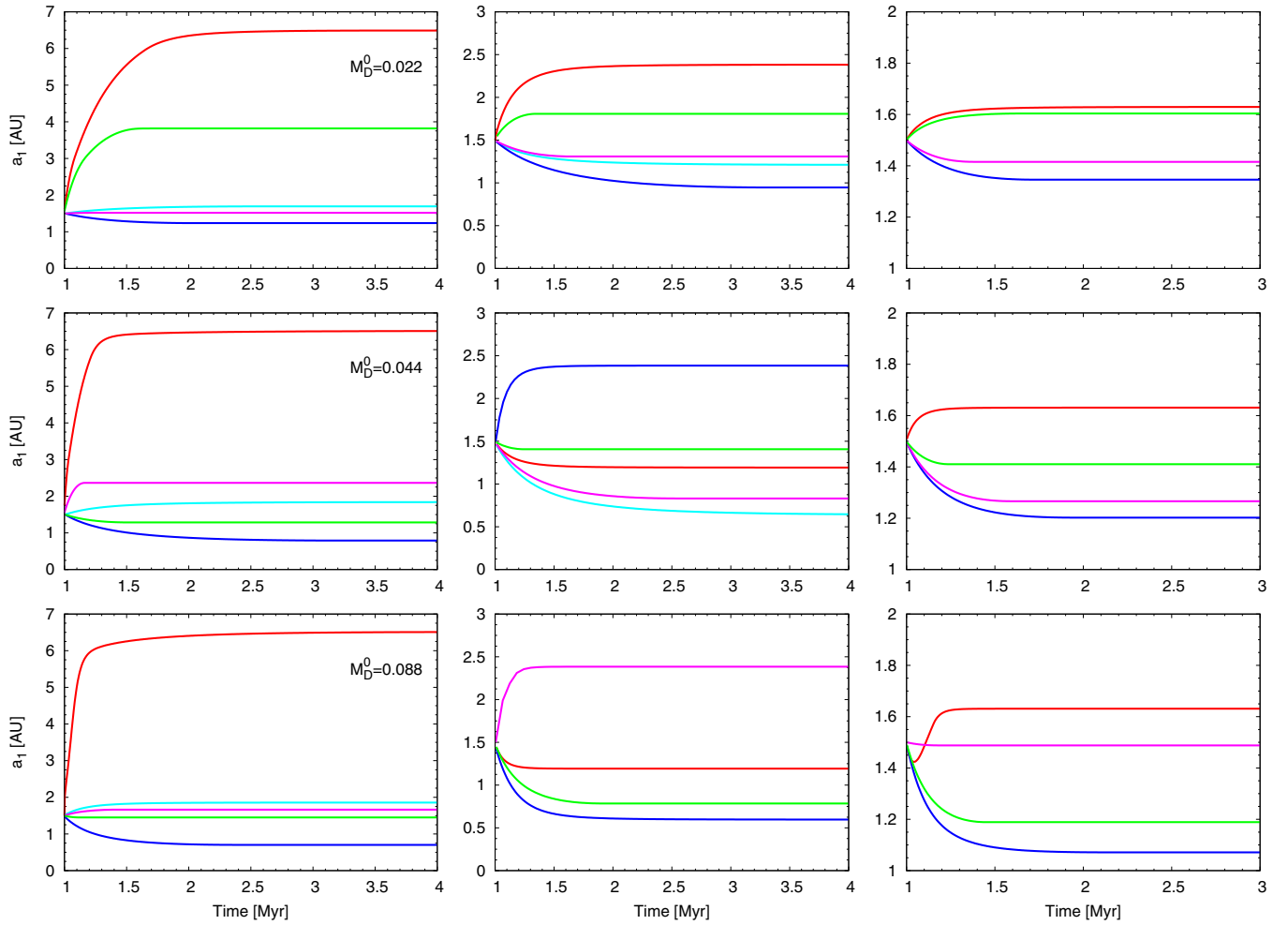


Figure 17. Evolution of the orbital radius (a_1) of the interior planet computed by integrating Equation (26) along with the disk models of Section 2.4 and assuming a formation timescale $\tau_p = 1$ Myr (see the text). The initial disk mass, in units of M_s , is indicated in the top-right corner of the left panels. The initial “slope” parameter of Σ is $\beta = 1/2$ (left), 1 (center), and $3/2$ (right). The curves in each panel refer to different values of ν_1 and f_{41} (see Table 2 to identify each curve). A complete list of the asymptotic values, a_∞ , is reported in Table 2. It is assumed that $a_2 = (3/2)^{2/3} a_1$.

(A color version of this figure is available in the online journal.)

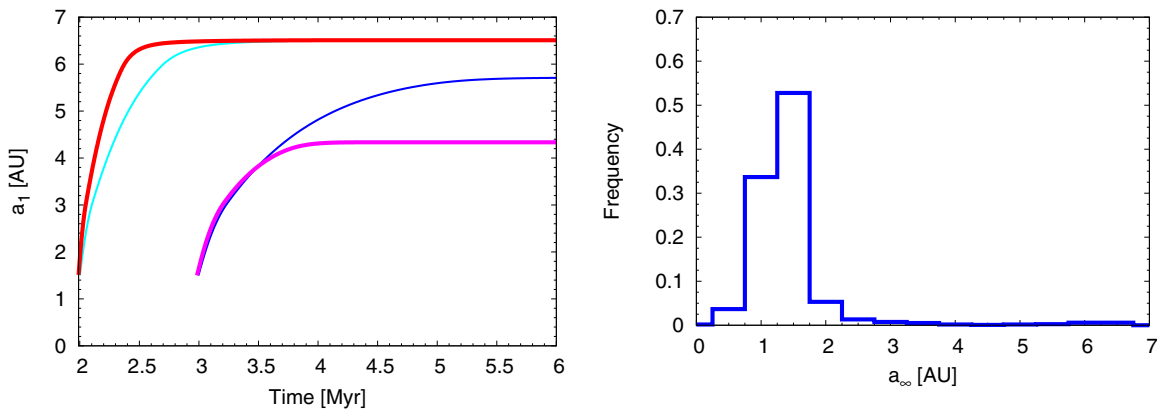


Figure 18. Left: orbital radius of the interior planet vs. time, assuming a formation timescale $\tau_p = 2$ and 3 Myr. Thin and thick curves represent, respectively, models with an initial disk mass $M_D^0 = 0.044$ ($f_{41} = 10$) and $0.088 M_s$ ($f_{41} = 100$). In all cases, parameters are $\beta = 1/2$ and $\nu_1 = 4 \times 10^{-6} r_1^2 \Omega_1$. For $\tau_p = 2$ and 3 Myr, these are the models that show the longest range of outward migration among those listed in Table 2. Right: histogram of the asymptotic orbital radius of the interior planet obtained by randomly varying the parameters ν_1 , f_{41} , and τ_p . See the text for further details.

(A color version of this figure is available in the online journal.)

the disk (see Lissauer et al. 2009 and references therein). In a disk with $H/r \gg 0.05$ or $\alpha_i \gg 0.005$, these rates would be comparable (DL08). Even assuming the same accretion rate for both planets, \dot{M}_p , the initial growth time, M_p/\dot{M}_p , of Saturn is

shorter than that of Jupiter, hence Saturn may approach the mass of Jupiter more or less quickly, depending on the local values of Σ and H/r . Furthermore, there is no obvious reason as to why Jupiter and Saturn should accrete gas at a disk-limited rate and

Table 2
Asymptotic Orbital Radii for $\tau_p = 1$ Myr

M_D^0/M_s	ν_1^c	a_∞^a								
		$\beta^b = 1/2$			$\beta = 1$			$\beta = 3/2$		
		$f_{41}^d = 10$	100	1000	1	10	100	0.1	1	10
0.022	4×10^{-6}	6.49	3.82	1.50	2.38	2.35	1.81	1.63	1.63	1.60
0.022	8×10^{-6}	1.70	1.52	1.50	1.21	1.30	1.50	1.35	1.41	1.50
0.022	1.6×10^{-5}	1.23	1.50	1.50	0.95	1.31	1.50
0.044	4×10^{-6}	6.51	6.50	2.37	...	2.38	2.37	1.63	1.63	1.63
0.044	8×10^{-6}	1.84	1.71	1.50	1.19	1.20	1.30	1.20	1.27	1.41
0.044	1.6×10^{-5}	0.79	1.28	1.50	0.64	0.83	1.41	1.50
0.088	4×10^{-6}	...	6.51	6.50	2.38	1.63	1.63	1.63
0.088	8×10^{-6}	...	1.86	1.66	1.19	1.19	1.19	1.07	1.10	1.19
0.088	1.6×10^{-5}	...	0.70	1.45	0.60	0.60	0.79	1.49	1.50	...

Notes.

^a Asymptotic value of the semimajor axis, in AU, of the interior planet's orbit.

^b Initial "slope" of the disk's surface density.

^c Kinematic viscosity at $r_1 = 1$ AU in units of $r_1^2 \Omega_1 = (GM_s r_1)^{1/2}$.

^d Rate of EUV ionizing photons emitted by the star in units of 10^{41} s^{-1} (see Equation (5)).

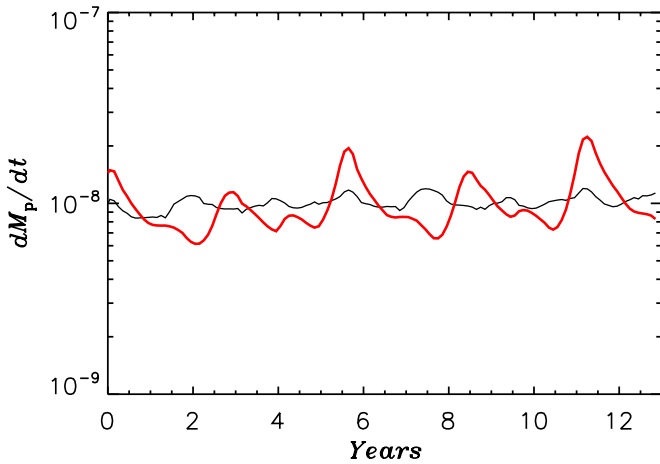


Figure 19. Disk-limited gas accretion rates, in units of $M_s \text{ yr}^{-1}$, of the interior (thin curve) and exterior (thick curve) planets. The pair is locked in the 3:2 mean motion resonance and the year count starts after about 6700 years of evolution. The plot shows only a small time interval to highlight the accretion modulation. The numerical resolution is such that there are $\sim 27^3$ and $\sim 20^3$ grid cells in the Hill sphere of the interior and exterior planets, respectively.

(A color version of this figure is available in the online journal.)

then suddenly stop accreting despite the continuing supply of gas from the disk.

The evolution of one high-resolution 3D calculation was continued by allowing the two planets to accrete gas following the procedure outlined in DL08, modified to account for the different local dynamical times⁶ (i.e., the timescale for mass removal depends on the planet's orbital frequency). Disk conditions are similar to those applied to the reference model of Section 3.3. The disk-limited accretion rates of the two planets are shown in Figure 19, where the thicker curve refers to the exterior planet. Both accretion rates are modulated (notice the logarithmic scale) over the orbital period due to the eccentric orbits (D'Angelo et al. 2006), although additional modulations may be present due to the resonant forcing. For conditions

⁶ If accretion proceeds through a disk around the planet, as suggested by the bottom-left panel of Figure 7, \dot{M}_p is equal to the rate at which the nebula supplies this disk, hence the connection with the orbital frequency.

simulated in Figure 19, the integrated values of \dot{M}_p are very similar, differing by less than 10%. These rates would yield a growth time for the exterior planet of a few times 10^4 years, typically much shorter than the migration time (see Figure 17). For comparison, the growth time of the interior planet would be $\sim 10^5$ years. The net effect of gas accretion could produce a mass ratio M_2/M_1 close to 1, or possibly larger (since gas starvation would likely occur for the interior planet first; see Figure 3).

The orbital evolution of the accreting planets, monitored over ~ 1000 years, does not show any significant deviation from the evolution of the non-accreting planets (the planet masses are fixed in this case, on account of the little variations expected over that timescale). However, as explained in Section 6, one or more accreting planets may change the steady-state structure of the inner disk, affecting the migration behavior of the planets.

6. GAS ACCRETION AND EFFECTS ON THE DISK

Resolving the problem of the rapid growth of the exterior planet, in a still relatively massive disk, would remove only one issue posed by gas accretion. In fact, even if Saturn suddenly stopped accreting, gas accretion onto Jupiter would continue to pose a problem. The issue here is not related to the growth of the interior planet's mass, but rather to the modification of the mass flux through the disk, across the planet's orbit.

As explained in Section 2.1, in a stationary disk the accretion rate is $\dot{M} = 3\pi\nu\Sigma$ and nearly independent of the radius r . Accretion on the interior (or exterior) planet would change \dot{M} . This phenomenon was analyzed in detail by Lubow & D'Angelo (2006, hereafter LD06) for the case of a single planet. The generalization to two planets can be performed by introducing an average accretion efficiency that quantifies the amount of gas accretion onto both planets, relative to an average local accretion rate through the disk.⁷ However, here we wish to consider the situation in which the interior planet accretes gas, but the exterior planet does not. Therefore, the formalism of LD06 can be applied in a straightforward manner. Let us indicate with $\dot{M}_e = \dot{M} = 3\pi\nu\Sigma$ the accretion rate sufficiently far from

⁷ As pointed out by LD06, for a given disk, there is a planet mass ($M_1 + M_2$, in this case) beyond which the couple exerted by the planet(s) will make the accretion disk evolve toward a decretion disk (Pringle 1991).

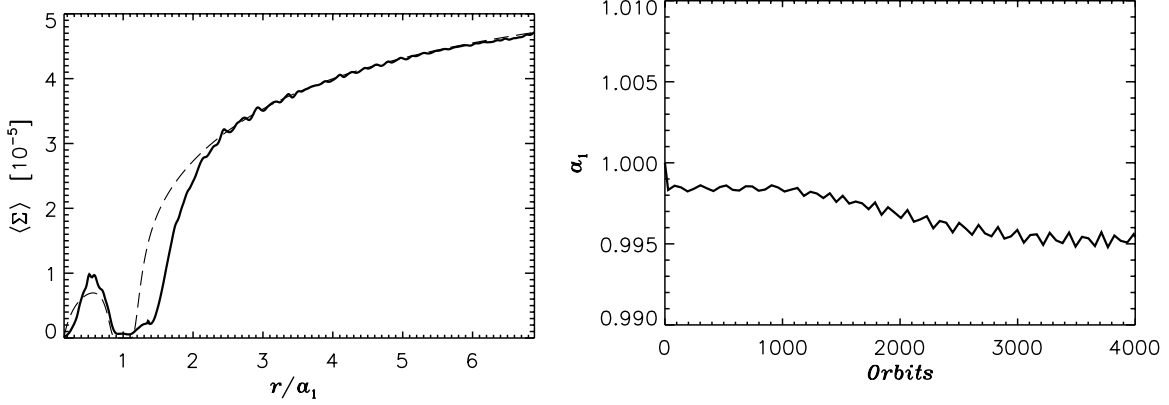


Figure 20. Left: azimuthally averaged surface density (solid line), in units of $M_s a_1^{-2}$, of a disk with a pair of planets, initially placed in the 3:2 commensurability. The exterior planet is non-accreting. The interior planet accretes gas with an efficiency parameter $\mathcal{E} \sim 6$ (see the text). The dashed line indicates the steady-state solution of LD06 (with a single planet) for $\mathcal{E} = 6$ and an inner disk radius of $0.15 a_1$. Right: migration track of the interior planet. Data are averaged over ~ 50 orbital periods. The planet begins migrating after 1000 (initial) orbits. The depletion of the inner disk (compare with Figure 8, long-dashed line) is sufficient to deactivate the outward migration mechanism (compare with Figure 11, top, which has different units on the time axis).

the exterior planet's orbit (so that it is basically unperturbed) and with \dot{M}_i the accretion rate inside the orbit of the interior planet. If there was no sink in the disk, then $\dot{M}_i = \dot{M}_e$. Yet, since some material is removed by the planet, in general $\dot{M}_i \leq \dot{M}_e$, which implies a reduction of Σ in the inner disk with respect to the same disk without the planet. This reduction depends on the planet's accretion efficiency \mathcal{E} , defined as the ratio of \dot{M}_p to the accretion rate interpolated at the planet's orbital radius. Since $\dot{M}_i = \dot{M}_e - \dot{M}_p$, one finds that $\dot{M}_i = \dot{M}_e / (\mathcal{E} + 1)$. This result formally applies if the disk's inner boundary, r_{\min} , is much smaller than a_1 . In general, one finds that (see LD06)

$$\dot{M}_i = \frac{\dot{M}_e}{1 + (1 - \sqrt{r_{\min}/a_1})\mathcal{E}}. \quad (28)$$

According to the Equation (28), the surface density in the inner disk is then expected to be reduced by a factor of the order of $\mathcal{E} + 1$ (assuming that ν remains unchanged), relative to the situation in which $\dot{M}_p = 0$. Accordingly, the (positive) Lindblad torque ($\propto \Sigma$, see Equation (21)) exerted by the inner disk on the (inner) planet is also expected to decrease. Such effect may slow down outward migration and may even tip the torque balance in favor of the negative torque acting on the interior planet.

We estimate the efficiency of accretion, \mathcal{E} , allowing for accretion on the interior planet only by applying the steady-state solution given by Equation (19) of LD06 as initial condition and using the iteration procedure outlined in LD06. The disk configuration is as that of the reference model in Section 3.3, except for a somewhat smaller disk's inner radius of $0.15 a_1$ and for the initial location of the exterior planet ($a_2/a_1 = 1.315$; see Figure 10). We find that $\mathcal{E} \sim 6$. There are fluctuations over time of both \dot{M}_p and \dot{M} (see Figure 19) and therefore the accretion efficiency is taken as the ratio of averaged quantities. The estimated variation is $\Delta\mathcal{E} \sim 1$. The accretion rate ratio is $\dot{M}_i/\dot{M}_e \sim 0.2$, whereas the corrected value, that is the ratio estimated for $r_{\min}/a_1 \ll 1$, is ~ 0.14 (see Equation (28)).

In Figure 20 (left panel), the surface density after 1000 orbits of the interior planet (solid line) is compared with the steady-state solution (Equation (19)) of LD06 for a disk with a single planet (dashed line). The reduced mass accretion past the planets, \dot{M}_i , results in a lower surface density (compare with the long-dashed line in the left panel of Figure 8). The migration of the resonant-orbit pair (initially placed in the 3:2 mean motion

resonance) in the stationary surface density of Figure 20 (left panel) is shown in the right panel. The reduced positive Lindblad torque by the inner disk cannot overcome the negative torque by the disk outside the planet's orbit, resulting in a migration speed $\dot{a}_1 \lesssim 0$ (note that the units of time in Figure 20 are initial orbits of the inner planet, not years).

7. THE 2:1 MEAN MOTION RESONANCE

A pair of planets undergoing convergent migration will first cross the 2:1 commensurability, before approaching the 3:2 mean motion resonance. While the latter resonant-orbit configuration may activate the outward migration mechanism discussed here (if $M_1/M_2 \approx 3$), the former may not (see Figures 6 and 16). But a pair of giant planets interacting with a gaseous disk can indeed be caught in this resonance, as shown by several studies (see, e.g., Kley 2003; Kley et al. 2004; Pierens & Nelson 2008; Zhang & Zhou 2010). We therefore seek conditions such that the outer planet may or may not overcome the barrier represented by capture in the 1:2 mean motion resonance, while migrating toward the inner planet.

In the case of convergent migration, the condition for capture of the exterior planet in a resonant orbit with the interior planet requires that the relative migration speed be such that

$$\left| \frac{da_{\text{rel}}}{dt} \right| < \frac{\Delta a_{\text{res}}}{T_l}, \quad (29)$$

where $\dot{a}_{\text{rel}} = \dot{a}_2 - \dot{a}_1$, Δa_{res} is the resonance amplitude in semimajor axis, and T_l is the resonant libration period, i.e., the period of the critical angle (e.g., Michtchenko et al. 2008) $\psi_1 = 2(\mathcal{M}_2 + \varpi_2) - (\mathcal{M}_1 + \varpi_1) - \varpi_1$, where \mathcal{M} indicates the mean anomaly and ϖ the argument of periapsis. Recall that in the case of a more massive interior planet, ψ_1 is a real resonant angle as it displays dynamical libration. For low-eccentricity orbits ($e \lesssim 0.1$), Mustill & Wyatt (2011; see also Quillen 2006) approximate the critical relative velocity for capture of the outer planet in the 1:2 mean motion resonance as

$$\left| \frac{da_{\text{rel}}}{dt} \right| \lesssim 1.2 \left(\frac{M_1}{M_s} \right)^{4/3} a_2 \Omega_2, \quad (30)$$

where it is assumed that $\Omega_1/\Omega_2 = 2$. Capture appears to be probabilistic at higher eccentricities, with a critical relative

velocity that becomes somewhat larger for larger eccentricities. Here we should stress, however, that the estimate of the critical velocity in Equation (30) assumes captures of “particles,” i.e., $M_1 \gg M_2$. If the planet transits the 1:2 orbital resonance with the interior planet, capture in the next first-order resonance, the 2:3, requires that $|\dot{a}_{\text{rel}}| \lesssim 14(M_1/M_s)^{4/3} a_2 \Omega_2$.

We shall assume that the inward migration speed of the interior planet is negligible compared to that of the exterior planet, thus $\dot{a}_{\text{rel}} \approx \dot{a}_2$. The exterior planet may, in principle, undergo a mode of rapid migration dominated by corotation torques (*type III*). D’Angelo & Lubow (2008) separated this mode of migration from type I mode by analyzing the torque density distributions and the fluid trajectories in the corotation region of the planet. They found that two conditions must be satisfied for the activation of type III migration. The first is that the migration timescale across the coorbital region is shorter than the timescale required to clear a gap over that same region. The second is that the unperturbed surface density at the planet location is such that

$$\left(\frac{a^2 \Sigma}{M_s}\right) \gtrsim \left(\frac{H}{a}\right)^2, \quad (31)$$

where disk quantities are sampled at $a = a_2$.⁸ If the first condition is fulfilled, the second condition requires that $\Sigma \gtrsim 10^{-3} M_s a^{-2}$ for $H/a \gtrsim 0.03$, which corresponds to a density in excess of 10^3 g cm^{-2} in the disk region within 3 AU of the star. According to Figures 4 and 5, this requirement is not met, thus we can assume that the outer planet migrates at a rate in between type I and type II migration rates. Assuming a speed of the order of type I and using Equation (24), one finds

$$\left|\frac{da_{\text{rel}}}{dt}\right| \sim \left(\frac{a}{H}\right)^2 \left(\frac{M_2}{M_s}\right) \left(\frac{a^2 \Sigma}{M_s}\right) a_2 \Omega_2, \quad (32)$$

all disk quantities being evaluated at $a = a_2$. In the equation above, a numerical factor of the order of unity multiplying the right-hand side is neglected. This is done to account for the fact that the density is partly depleted and the actual migration rate deviates somewhat from the type I rate (see DL08). Moreover, we find that Equation (32) gives a reasonable order-of-magnitude approximation to numerical results.

Therefore, capture of the exterior planet in the 1:2 mean motion resonance with the interior planet may occur if the unperturbed surface density is lower than a critical value, so that

$$\left(\frac{a^2 \Sigma}{M_s}\right) \lesssim \left(\frac{M_1}{M_s}\right)^{4/3} \left(\frac{H}{a}\right)^2 \left(\frac{M_s}{M_2}\right). \quad (33)$$

If $H/a \gtrsim 0.03$, then a surface density $\Sigma \lesssim 3 \times 10^{-4} M_s a^{-2}$, or about 650 g cm^{-2} at $\approx 2 \text{ AU}$, may be sufficient to allow for capture in this resonance. If the exterior planet crossed the 1:2 commensurability while it had a much lower mass, say ~ 20 Earth masses, this critical density would not decrease, even accounting for a numerical factor of 4–5 in Equation (32) and restoring a full type I migration.

The inequality in Equation (33) suggests that if $a_2^2 \Sigma / M_s \gtrsim 5 \times 10^{-4}$ in a disk with $H/r \sim 0.04$, the exterior planet may

⁸ The condition represented by Equation (31) is also consistent with the case reported by Masset & Snellgrove (2001), which show an exterior planet migration dominated by corotation torques. In that case, $a_1^2 \Sigma / M_s = 6 \times 10^{-4}$, $H/r = 0.04$, and $a_2 = 2$ (in their units). Hence, evaluating at the initial position of the exterior planet, one has $a_2^2 \Sigma / M_s = 2.4 \times 10^{-3} > (H/a_2)^2$.

transit the 1:2 mean motion resonance with the interior planet. These conditions are realized, for example, in the model of Masset & Snellgrove (2001, see their Figure 1) and in the models of Pierens & Nelson (2008, see their Figure 5), considering that the density must be rescaled at the radius of the resonance crossing, where $a_2 \approx 1.5$ (in the units of Masset & Snellgrove 2001) and $a_2 \approx 1.3$ (in the units of Pierens & Nelson 2008). The solar nebula models considered here, however, suggest that if the orbits approach the 1:2 commensurability in the inner disk, after $\sim 1 \text{ Myr}$, then capture is likely in a statistical sense (see Figure 5).

Equation (33) represents only an approximate condition for resonance locking because orbital eccentricity may play some role and because Equation (30) was not derived for the capture of similar mass bodies. In order to provide a further test on conditions that may lead to locking of the exterior planet in the 1:2 commensurability, calculations along the lines of those presented in Section 3.3 are performed for varying initial surface density at 1 AU, Σ_1 . The disk conditions are those used for the reference model in Figure 11, except that the exterior planet is placed initially on a circular orbit at a distance of 2.8 AU from the star, outside the resonance location with the interior planet, and both begin migrating after 500 years. Results from these calculations are illustrated in Figure 21, which shows the ratio of the mean motions. The top panel refers to values of Σ_1 compatible with those found in the disk evolution models at the time of planet formation (see Figure 5, left). In these cases, the exterior planet becomes locked in the 1:2 orbital resonance. Since $\dot{\Omega} = -(3/2)\Omega\dot{a}/a$, assuming that Ω_1 is nearly constant, then

$$\frac{d}{dt} \left(\frac{\Omega_1}{\Omega_2}\right) \sim -\frac{3}{2} \left(\frac{\Omega_1}{\Omega_2}\right) \left(\frac{a}{H}\right)^2 \left(\frac{M_2}{M_s}\right) \left(\frac{a^2 \Sigma}{M_s}\right) \Omega_2, \quad (34)$$

where quantities depending on a are evaluated at $a = a_2$. Predictions from Equation (34) are superimposed (circles) to Ω_1/Ω_2 curves in Figure 21, indicating that the exterior planet does approach the interior planet, at least initially, with a radial speed on the order of the relative velocity given by Equation (32).

The bottom panel of Figure 21 shows cases with higher initial densities in which capture of the exterior planet is in the 1:2 or the 2:3 orbital resonance. There is overall agreement with Equation (33), and transit across the 1:2 orbital resonance is obtained for $r_1^2 \Sigma_1 / M_s = 6 \times 10^{-4}$. We did not investigate the exact density value at which locking transitions from one to the other resonant configuration, but it is likely that there exists an interval of values for which the result is stochastic.

The inset in the top panel of Figure 21 illustrates the migration of the interior planet after resonance locking. In the bottom panel, migration is outward for the case that shows locking of the exterior planet in the 2:3 mean motion resonance with the interior planet, inward in the other cases. These results confirm what was argued above and suggested by Figures 6 and 16: the 2:3 orbital resonance leads to outward migration, the 1:2 resonance does not.

A small disk aspect ratio may help preventing capture of the exterior planet in the 1:2 commensurability with the interior planet. However, the condition for gap formation (Equation (22)) suggests that the migration of the exterior planet may transition to type II, and \dot{a}_1 cannot be neglected. In this case, since $v \propto a^\beta$ and $\dot{a} \sim v/a \propto a^{\beta-1}$, convergent migration requires that $\beta > 1$. By applying Equation (30), one finds that if the kinematic viscosity at 1 AU is $\nu_1 \lesssim (M_1/M_s)^{4/3} (1 \text{ AU}/a_2)^{(\beta-1/2)}$ then convergent type II migration may still lead to orbital locking

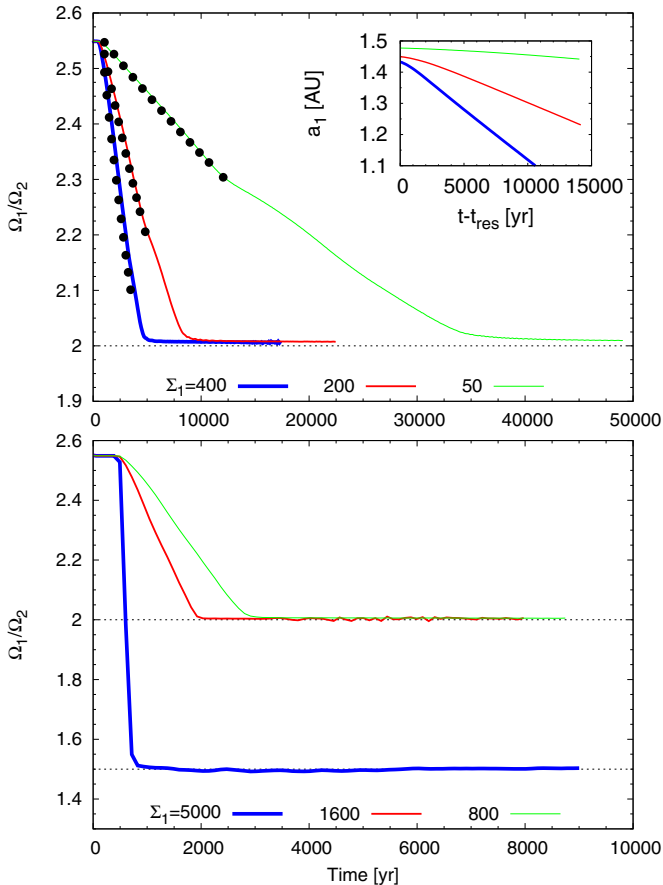


Figure 21. Ratio of the mean motions vs. time for a pair of planets undergoing convergent migration. The value of the disk’s surface density at 1 AU is indicated at the bottom of each panel, in units of g cm^{-2} , for the curves of different thickness. The top panel illustrates evolutions for typical densities obtained from the disk models of Section 2.4. Circles are predictions from Equation (34). The inset shows the migration tracks of the interior planet after resonance locking occurs. At higher densities, capture of the exterior planet transitions from the 1:2 to the 2:3 commensurability, as illustrated in the bottom panel.

(A color version of this figure is available in the online journal.)

in the 1:2 mean motion resonance. However, this estimate is complicated by the fact that if the planet mass becomes larger than the local disk mass, a likely situation at late evolutionary times, \dot{a} is also proportional to $a^2 \Sigma / M_p$ due to intervening inertia effects (see, e.g., Syer & Clarke 1995; Ivanov et al. 1999). Hence, the interior planet would likely slow down before the exterior planet would.

7.1. Saturn Formation within the 1:2 Orbital Resonance with Jupiter

We shall consider here the possibility that Saturn forms within the 1:2, but outside the 2:3, commensurability with Jupiter, while both planets are beyond several AU from the Sun. If during the course of its evolution Saturn remains inside the 1:2 mean motion resonance with Jupiter, then capture in the 2:3 orbital resonance is still possible.

In order to maintain such a compact orbital configuration throughout the evolution of the two planets, the migration rates must be very similar over time. In fact, if the constraint $1.31 < a_2/a_1 < 1.59$ has to be preserved, a change of this ratio of at most 20% over the formation timescales essentially implies that a_2/a_1 is roughly constant. Therefore, by taking the

time derivative, one has

$$\frac{\dot{a}_2}{a_2} \sim \frac{\dot{a}_1}{a_1}. \quad (35)$$

But since the interior planet has to grow faster than the exterior planet does, their migration rates are bound to differ, at some point in time at least. Thus, the condition in Equation (35) is unlikely to be (always) satisfied and the difference $a_2 - a_1$ will either increase or decrease.

If Saturn forms within the 1:2 orbital resonance and Jupiter has still to acquire most of its mass, there will be a phase when the migration rate of Jupiter significantly exceeds that of Saturn (presumably, around the time of runaway gas accretion; see DL08). Hence, it is most likely that Saturn is left behind and probably becomes trapped in the 1:2 commensurability. Instead, if Jupiter has already acquired the bulk of its mass, the opposite is likely to occur and most probably Saturn becomes locked in the 2:3 orbital resonance while it is still growing.

We consider this last situation in some detail by performing 3D calculations similar to those of the reference model of Section 3.3, but applying a lower mass to the exterior planet: $q = M_2/M_s = 10^{-4}$ and 2×10^{-4} . Equation (27), appropriately modified for mass ratios $q \neq q_{\text{ref}}$ (see the discussion after Equation (27)), suggests that if $q \approx 10^{-4}$ migration of the pair is inward, but if $q \approx 2 \times 10^{-4}$ then migration is outward. Direct calculations agree with these predictions, as indicated by the cumulative torques shown in the top-left panel of Figure 22 for three different values of M_2 (see the caption for details). The density depletion due to the tidal torques of the exterior planet amounts to $\sim 35\%$ for $M_2 = 10^{-4} M_s$ and to $\sim 60\%$ for $M_2 = 2 \times 10^{-4} M_s$ (top-right panel), in accord with the expectations of Equation (22). The bottom panels of Figure 22 show vertical distributions of the mass density (see the figure caption).

Therefore, if Saturn grows while locked in the 2:3 orbital resonance with Jupiter, there is a mass smaller than Saturn’s final mass for which migration stalls and then reverses, as suggested by \mathcal{T}_{CM} as function of M_2 in Figure 22 (top-left panel). This situation would prevent Jupiter from reaching the inner disk regions, unless Saturn achieved the mass for migration reversal when Jupiter is already there. For $H/r \approx 0.04$, such mass is between $10^{-4} M_s$ and $2 \times 10^{-4} M_s$ (and presumably closer to $10^{-4} M_s$ for $H/r \approx 0.03$), which implies that a substantial fraction of Saturn’s envelope is acquired in the inner regions of the solar nebula.

This circumstance, however, would likely be at odds with the elemental abundances of some species measured in Saturn’s atmosphere (see Hersant et al. 2008). The abundances relative to hydrogen of elements such as C, N, S, As, and P are a few to several times as high as the solar abundances (see Lodders 2003; Asplund et al. 2009 and references therein). In fact, the presence in large amount of these elements is believed to have arisen from accretion of gas (e.g., Guillot & Hueso 2006) and/or solids (e.g., Hersant et al. 2008) in a cold disk environment.

8. SUMMARY AND DISCUSSION

This paper presents results of thermodynamical models of protoplanetary disks that are constructed by applying ranges of parameters that may have characterized the early solar nebula (see Section 2). Disk evolution is driven by viscous torques and photoevaporation originating from the central star (see Section 2.1). Thermal balance in the disk is achieved by equating

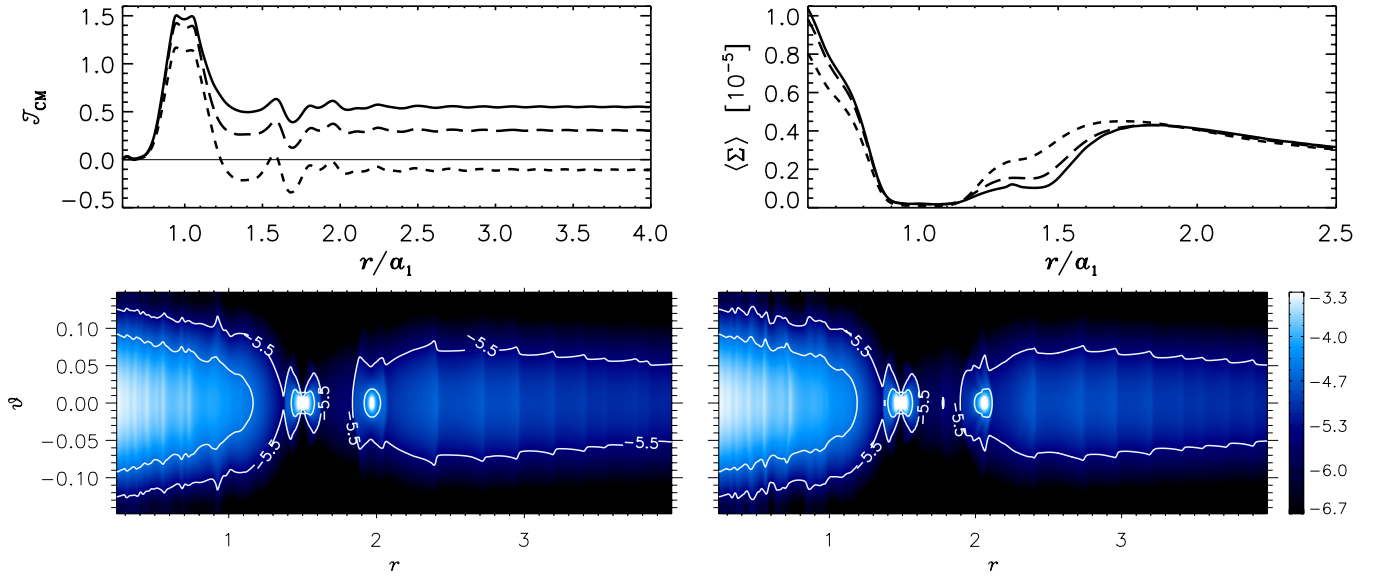


Figure 22. Top: cumulative torques (left) exerted on the interior planet and averaged surface density (right), obtained from 3D calculations whose parameters are as in the reference model of Section 3.3. Different lines types indicate different masses of the exterior planet (M_2/M_s): 2.9×10^{-4} (solid), 2×10^{-4} (long-dashed), and 10^{-4} (short-dashed). The torque is normalized to $10^{-3} GM_s^2 (M_1/M_s)^2 / a_1$ and Σ is in units of $M_s r_1^{-2}$. Bottom: vertical stratification of the mass density at disk azimuth $\phi_j = \phi_s$, in units of $M_s r_1^{-3}$, for $M_2 = 10^{-4} M_s$ (left) and $2 \times 10^{-4} M_s$ (right).

(A color version of this figure is available in the online journal.)

viscous and stellar irradiation heating with radiative cooling in the vertical direction (see Section 2.2). Only models that predict disk lifetimes between 1 and 20 Myr are considered viable representations of the solar nebula (see Table 1), in line with observations and core-nucleated accretion calculations of gas giants. Such models provide the physical conditions (see, e.g., Figure 3) at the time and after the planets acquired most of their mass (see Section 2.4) and can be used to simulate their long-term orbital migration.

2D and 3D hydrodynamical calculations are used to quantify the migration rates of a pair of planets with mass ratios corresponding to Jupiter’s and Saturn’s, $M_1/M_s \approx 10^{-3}$ and $M_2/M_s \approx 3 \times 10^{-4}$ (see Section 3). The orbits of the planets are initially placed in proximity of the 3:2 mean motion resonance (see, e.g., Figure 7). As described by Masset & Snellgrove (2001), a necessary condition to activate outward migration is the overlap of the tidal gap carved in the disk by a less massive, exterior planet with the gap of the more massive, interior planet (see Figure 8). The relative depth and width of the gaps provide the sufficient condition (see Section 3.2). High temperatures and kinematic viscosities inhibit gap formation, either promoting inward migration (see Section 3.3) or stopping outward migration (see Section 3.4).

If a near 3:2 commensurability is preserved, there are stalling radii in the disk, toward which the pair will converge (see Figure 14). In general, to first approximation, these radii depend on a combination of the turbulence viscosity parameter, disk thickness, and mass of the outer planet (see Figures 15 and 22).

For planets moving outward from the inner disk region ($r \lesssim 2$ AU) at a time between 1 and 3 Myr, the interior planet may reach beyond ~ 5 AU only if viscosity is low enough, the surface density is not too steep, and the disk not too warm (see Section 4). However, the probability for this to happen appears to be low (see Table 2). Experiments performed on random samples of the parameter space suggest that in 98% of the cases the interior planet stops within 4 AU (see Figure 18).

At least three requirements must be satisfied to establish and maintain the 3:2 commensurability and hence promote

outward migration: (1) the exterior planet must stop growing (see Section 5), (2) the interior planet must do the same (see Section 6), and (3) the relative migration speed prior to capture must be large, so that the exterior planet can transit the 1:2 orbital resonance (see Section 7). If requirement (1) is violated, the mass ratio M_2/M_1 may approach 1 on a timescale shorter than the migration timescale (see Figure 19), and the outward motion is interrupted. If requirement (2) is violated, the accretion rate through the disk, past the interior planet, is reduced. The surface density inside the orbit of the inner planet drops and so does the positive Lindblad torque exerted on the planet, inhibiting outward migration (see Figure 20). If requirement (3) is violated, migration is not reversed and both planets continue moving toward the star (see Figure 21). The 1:2 orbital resonance may still induce outward migration, but at masses larger than Jupiter’s and Saturn’s (see Figure 16).

The outward migration mechanism is operable, as also argued in previous studies, but the limitations can be severe. In particular, it is difficult to reconcile the absence of accretion on both giant planets with the presence of gas around the planets (see, e.g., Lissauer et al. 2009 and references therein). Two processes capable of shutting down the accretion of gas must be invoked although, in principle, they need not be different. Additionally, since envelope collapse begins once the envelope mass exceeds the core mass, it is reasonable to assume that before growth stops both planets were undergoing runaway gas accretion, i.e., digesting all the gas the nebula could provide. Presumably, the sought processes are not “internal,” i.e., related to the structure of the envelopes, because otherwise they would likely occur around similar envelope masses,⁹ which is obviously not the case. But if the processes are of an “external” nature, i.e., related to the supply of gas, then the interior planet would probably undergo through said process before the exterior planet would, since disk gas removal within several AU proceeds

⁹ The fast contraction phase that initiates runaway gas accretion is not much influenced by boundary conditions, i.e., by the thermodynamical state of the disk. Furthermore, given the compact orbital configuration of the planets, it is unlikely that disk conditions would be very different at the two locations.

from the inside out. Therefore, it seems as though the problem of stopping gas accretion on both planets does not admit a trivial solution.

The transit of the exterior planet across the 1:2 commensurability with the interior planet, within a few AU of the star, requires surface densities far in excess of those predicted by the disk evolution models constructed here. The 1:2 resonant-orbit configuration is then favored, in a statistical sense, over the 2:3 one. It is worth mentioning that core-nucleated accretion models necessitate high enough surface densities of solid material, but in the form of planetesimals not of dust. Since it takes time to turn dust into planetesimals and the gaseous disk evolves during that time, dust-to-gas mass ratios do not provide useful information about gas densities at the time giant planets acquired most of their gaseous contents. Disk-limited accretion rates depend linearly on the gas surface density, but tend to be rather large. At ~ 5 AU, if Σ was of the order of 10 g cm^{-2} around the time of the runaway gas accretion phase, it would take $\sim 10^5$ years to deliver over one-half of the current mass of Jupiter (see, e.g., Lissauer et al. 2009 and references therein). At ~ 9 AU, a few g cm^{-2} would be sufficient to deliver about a Saturn mass worth of gas in $\sim 10^5$ years. Hence, it is reasonable to assume that low gas densities in the solar nebula do not prevent the giant planets from reaching their final masses.

Even though it appears unlikely that Saturn can transit the 1:2 commensurability with Jupiter in an evolved nebula, there is the possibility that it forms within this orbital resonance. In such case, however, we argue (see Section 7.1) that it may be difficult for the pair to reach the 1–2 AU disk region. In fact, capture in the 2:3 mean motion resonance with Jupiter and ensuing migration reversal can occur before Saturn attains its full mass (see Figure 22), probably when it has between about 1/3 and 2/3 of the final mass.

We thank the referee for a prompt response and helpful suggestions. G.D. thanks the Los Alamos National Laboratory for its hospitality. G.D. acknowledges support from NASA Outer Planets Research Program grant 202844.02.02.01.75 and from NASA Origins of Solar Systems Program grants NNX11AD20G and NNX11AK54G. Resources supporting this work were provided by the NASA High-End Computing (HEC) Program through the NASA Advanced Supercomputing (NAS) Division at Ames Research Center.

REFERENCES

- Alexander, R. D., Clarke, C. J., & Pringle, J. E. 2005, *MNRAS*, **358**, 283
- Alibert, Y., Mousis, O., Mordasini, C., & Benz, W. 2005, *ApJ*, **626**, L57
- Armitage, P. J. 2011, *ARA&A*, **49**, 195
- Asplund, M., Grevesse, N., Sauval, A. J., & Scott, P. 2009, *ARA&A*, **47**, 481
- Bath, G. T., & Pringle, J. E. 1981, *MNRAS*, **194**, 967
- Benvenuto, O. G., Fortier, A., & Brunini, A. 2009, *Icarus*, **204**, 752
- Beutler, G. 2005, *Methods of Celestial Mechanics, Vol. I: Physical, Mathematical, and Numerical Principles*, ed. G. Beutler (Berlin: Springer)
- Brent, R. P. 1973, *Algorithms for Minimization Without Derivatives* (Englewood Cliffs, NJ: Prentice-Hall)
- Bromley, B. C., & Kenyon, S. J. 2011, *ApJ*, **731**, 101
- Chambers, J. E. 2009, *ApJ*, **705**, 1206
- Chiang, E., & Youdin, A. N. 2010, *Annu. Rev. Earth Planet. Sci.*, **38**, 493
- Chiang, E. I., & Goldreich, P. 1997, *ApJ*, **490**, 368
- Clarke, C. 2011, in *The Dispersal of Disks around Young Stars*, ed. P. J. V. Garcia (Chicago, IL: Univer. Chicago Press), 355
- Crida, A., Masset, F., & Morbidelli, A. 2009, *ApJ*, **705**, L148
- D'Alessio, P., Canto, J., Calvet, N., & Lizano, S. 1998, *ApJ*, **500**, 411
- D'Angelo, G., Bate, M. R., & Lubow, S. H. 2005, *MNRAS*, **358**, 316
- D'Angelo, G., Henning, T., & Kley, W. 2003, *ApJ*, **599**, 548
- D'Angelo, G., & Lubow, S. H. 2008, *ApJ*, **685**, 560 (DL08)
- D'Angelo, G., Lubow, S. H., & Bate, M. R. 2006, *ApJ*, **652**, 1698
- Davis, S. S. 2005, *ApJ*, **627**, L153
- de Val-Borro, M., Edgar, R. G., Artymowicz, P., et al. 2006, *MNRAS*, **370**, 529
- Dodson-Robinson, S. E., Bodenheimer, P., Laughlin, G., et al. 2008, *ApJ*, **688**, L99
- Dullemond, C. P., Hollenbach, D., Kamp, I., & D'Alessio, P. 2007, in *Protostars and Planets V*, ed. B. Reipurth, D. Jewitt, & K. Keil (Tucson, AZ: Univ. Arizona Press), 555
- Ferguson, J. W., Alexander, D. R., Allard, F., et al. 2005, *ApJ*, **623**, 585
- Fernandez, J. A., & Ip, W.-H. 1984, *Icarus*, **58**, 109
- Franklin, F. A., Lewis, N. K., Soper, P. R., & Holman, M. J. 2004, *AJ*, **128**, 1391
- Gammie, C. F. 2001, *ApJ*, **553**, 174
- Gladman, B. 1993, *Icarus*, **106**, 247
- Gomes, R., Levison, H. F., Tsiganis, K., & Morbidelli, A. 2005, *Nature*, **435**, 466
- Gorti, U., Dullemond, C. P., & Hollenbach, D. 2009, *ApJ*, **705**, 1237
- Gorti, U., & Hollenbach, D. 2009, *ApJ*, **690**, 1539
- Guillot, T., & Hueso, R. 2006, *MNRAS*, **367**, L47
- Hahn, J. M., & Malhotra, R. 1999, *AJ*, **117**, 3041
- Hairer, E., Nørsett, S. P., & Wanner, G. 1993, *Solving Ordinary Differential Equations I: Nonstiff Problems* (2nd ed.; Springer Series in Computational Mathematics, Vol. 8; Berlin: Springer)
- Haisch, K. E., Lada, E. A., & Lada, C. J. 2001, *ApJ*, **553**, L153
- Hartmann, L., Zhu, Z., & Calvet, N. 2011, arXiv:1106.3343
- Hayashi, C. 1981, *Prog. Theor. Phys. Suppl.*, **70**, 35
- Hersant, F., Gautier, D., Tobie, G., & Lunine, J. I. 2008, *Planet. Space Sci.*, **56**, 1103
- Hubeny, I. 1990, *ApJ*, **351**, 632
- Hubickyj, O., Bodenheimer, P., & Lissauer, J. J. 2005, *Icarus*, **179**, 415
- Hueso, R., & Guillot, T. 2005, *A&A*, **442**, 703
- Ivanov, P. B., Papaloizou, J. C. B., & Polnarev, A. G. 1999, *MNRAS*, **307**, 79
- Kenyon, S. J., & Bromley, B. C. 2009, *ApJ*, **690**, L140
- Kley, W. 2003, *Celest. Mech. Dyn. Astron.*, **87**, 85
- Kley, W., Bitsch, B., & Klahr, H. 2009, *A&A*, **506**, 971
- Kley, W., Peitz, J., & Bryden, G. 2004, *A&A*, **414**, 735
- Lin, D. N. C., & Papaloizou, J. 1986a, *ApJ*, **307**, 395
- Lin, D. N. C., & Papaloizou, J. 1986b, *ApJ*, **309**, 846
- Lissauer, J. J., Hubickyj, O., D'Angelo, G., & Bodenheimer, P. 2009, *Icarus*, **199**, 338
- Lodders, K. 2003, *ApJ*, **591**, 1220
- Lubow, S. H., & D'Angelo, G. 2006, *ApJ*, **641**, 526 (LD06)
- Lubow, S. H., & Ida, S. 2010, in *Planet Migration*, ed. S. Seager (Tucson, AZ: Univ. Arizona Press), 347
- Lynden-Bell, D., & Pringle, J. E. 1974, *MNRAS*, **168**, 603
- Malhotra, R. 1993, *Nature*, **365**, 819
- Malhotra, R. 1995, *AJ*, **110**, 420
- Masset, F. 2000, *A&AS*, **141**, 165
- Masset, F., & Snellgrove, M. 2001, *MNRAS*, **320**, L55
- Masset, F. S. 2002, *A&A*, **387**, 605
- Menou, K., & Goodman, J. 2004, *ApJ*, **606**, 520
- Michtchenko, T. A., Beaugé, C., & Ferraz-Mello, S. 2008, *MNRAS*, **391**, 215
- Mihalas, D., & Weibel Mihalas, B. 1999, *Foundations of Radiation Hydrodynamics* (New York: Dover)
- Minton, D. A., & Malhotra, R. 2009, *Nature*, **457**, 1109
- Morbidelli, A., & Crida, A. 2007, *Icarus*, **191**, 158
- Morbidelli, A., Levison, H. F., Tsiganis, K., & Gomes, R. 2005, *Nature*, **435**, 462
- Mordasini, C., Alibert, Y., Klahr, H., & Benz, W. 2011, in *Detection and Dynamics of Transiting Exoplanets*, St. Michel l'Observatoire, France, ed. F. Bouchy, R. Díaz, & C. Moutou (EPJ Web of Conferences, Vol. 11) 4001
- Movshovitz, N., Bodenheimer, P., Podolak, M., & Lissauer, J. J. 2010, *Icarus*, **209**, 616
- Müller, T. W. A., Kley, W., & Meru, F. 2012, *A&A*, **541**, A123
- Mustill, A. J., & Wyatt, M. C. 2011, *MNRAS*, **413**, 554
- Nelson, R. P., Papaloizou, J. C. B., Masset, F., & Kley, W. 2000, *MNRAS*, **318**, 18
- Papaloizou, J., & Lin, D. N. C. 1984, *ApJ*, **285**, 818
- Pierens, A., & Nelson, R. P. 2008, *A&A*, **482**, 333
- Pierens, A., & Raymond, S. N. 2011, *A&A*, **533**, A131
- Pollack, J. B., Hollenbach, D., Beckwith, S., et al. 1994, *ApJ*, **421**, 615
- Pollack, J. B., Hubickyj, O., Bodenheimer, P., et al. 1996, *Icarus*, **124**, 62
- Press, W. H., Teukolsky, S. A., Vetterling, W. T., & Flannery, B. P. 1992, *Numerical Recipes in FORTRAN: The Art of Scientific Computing* (2nd ed.; Cambridge: Cambridge Univ. Press)
- Pringle, J. E. 1981, *ARA&A*, **19**, 137
- Pringle, J. E. 1991, *MNRAS*, **248**, 754

- Quillen, A. C. 2006, *MNRAS*, **365**, 1367
- Rafikov, R. R., & De Colle, F. 2006, *ApJ*, **646**, 275
- Roberge, A., & Kamp, I. 2010, in *Protoplanetary and Debris Disks*, ed. S. Seager (Tucson, AZ: Univ. Arizona Press), 269
- Ruden, S. P., & Pollack, J. B. 1991, *ApJ*, **375**, 740
- Scott, E. R. D. 2006, *Icarus*, **185**, 72
- Shakura, N. I., & Syunyaev, R. A. 1973, *A&A*, **24**, 337
- Siess, L., Dufour, E., & Forestini, M. 2000, *A&A*, **358**, 593
- Stone, J. M., & Norman, M. L. 1992, *ApJS*, **80**, 753
- Syer, D., & Clarke, C. J. 1995, *MNRAS*, **277**, 758
- Tsiganis, K., Gomes, R., Morbidelli, A., & Levison, H. F. 2005, *Nature*, **435**, 459
- Walsh, K. J., Morbidelli, A., Raymond, S. N., O'Brien, D. P., & Mandell, A. M. 2011, *Nature*, **475**, 206
- Ward, W. R. 1986, *Icarus*, **67**, 164
- Ward, W. R., & Hahn, J. M. 2000, in *Protostars and Planets IV*, ed. V. Mannings, A. P. Boss, & S. S. Russell (Tucson, AZ: Univ. Arizona Press), 1135
- Weidenschilling, S. J. 1977, *Ap&SS*, **51**, 153
- Williams, J. P., & Cieza, L. A. 2011, *ARA&A*, **49**, 67
- Zhang, H., & Zhou, J.-L. 2010, *ApJ*, **714**, 532